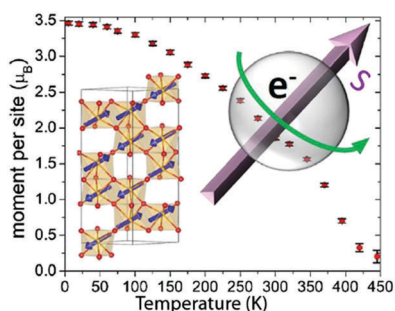


We have presented the Graphical Abstract text and image for your article below. This brief summary of your work will appear in the contents pages of the issue in which your article appears.



MnFe_{0.5}Ru_{0.5}O₃: an above-room-temperature antiferromagnetic semiconductor

Xiaoyan Tan, Emma E. McCabe, Fabio Orlandi, Pascal Manuel, Maria Batuk, Joke Hadermann, Zheng Deng, Changqing Jin, Israel Nowik, Rolfe Herber, Carlo U. Segre, Sizhan Liu, Mark Croft, Chang-Jong Kang, Saul Lapidus, Corey E. Frank, Haricharan Padmanabhan, Venkatraman Gopalan, Meixia Wu, Man-Rong Li, Gabriel Kotliar, David Walker and Martha Greenblatt*

MnFe_{0.5}Ru_{0.5}O₃ is discovered at high pressure high temperature as an above-room-temperature antiferromagnetic semiconductor for potential spintronic application.

Please check this proof carefully. Our staff will not read it in detail after you have returned it.

Please send your corrections either as a copy of the proof PDF with electronic notes attached or as a list of corrections. **Do not edit the text within the PDF or send a revised manuscript** as we will not be able to apply your corrections. Corrections at this stage should be minor and not involve extensive changes.

Proof corrections must be returned as a single set of corrections, approved by all co-authors. No further corrections can be made after you have submitted your proof corrections as we will publish your article online as soon as possible after they are received.

Please ensure that:

- The spelling and format of all author names and affiliations are checked carefully. You can check how we have identified the authors' first and last names in the researcher information table on the next page. **Names will be indexed and cited as shown on the proof, so these must be correct.**
- Any funding bodies have been acknowledged appropriately and included both in the paper and in the funder information table on the next page.
- All of the editor's queries are answered.
- Any necessary attachments, such as updated images or ESI files, are provided.

Translation errors can occur during conversion to typesetting systems so you need to read the whole proof. In particular please check tables, equations, numerical data, figures and graphics, and references carefully.

Please return your **final** corrections, where possible within **48 hours** of receipt, by e-mail to: materialsC@rsc.org. If you require more time, please notify us by email.

Funding information

Providing accurate funding information will enable us to help you comply with your funders' reporting mandates. Clear acknowledgement of funder support is an important consideration in funding evaluation and can increase your chances of securing funding in the future.

We work closely with Crossref to make your research discoverable through the Funding Data search tool (<http://search.crossref.org/funding>). Funding Data provides a reliable way to track the impact of the work that funders support. Accurate funder information will also help us (i) identify articles that are mandated to be deposited in **PubMed Central (PMC)** and deposit these on your behalf, and (ii) identify articles funded as part of the **CHORUS** initiative and display the Accepted Manuscript on our web site after an embargo period of 12 months.

Further information can be found on our webpage (<http://rsc.li/funding-info>).

What we do with funding information

We have combined the information you gave us on submission with the information in your acknowledgements. This will help ensure the funding information is as complete as possible and matches funders listed in the Crossref Funder Registry.

If a funding organisation you included in your acknowledgements or on submission of your article is not currently listed in the registry it will not appear in the table on this page. We can only deposit data if funders are already listed in the Crossref Funder Registry, but we will pass all funding information on to Crossref so that additional funders can be included in future.

Please check your funding information

The table below contains the information we will share with Crossref so that your article can be found *via* the Funding Data search tool. **Please check that the funder names and grant numbers in the table are correct and indicate if any changes are necessary to the Acknowledgements text.**

| Funder name | Funder's main country of origin | Funder ID (for RSC use only) | Award/grant number |
|--|---------------------------------|------------------------------|--------------------------------------|
| Division of Materials Research | United States | 100000078 | NSF-DMR-1507252 |
| U.S. Department of Energy | United States | 100000015 | DE-AC02-06CH11357, DE-FOA-0001276 |
| National Science Foundation | United States | 100000001 | DMR-1820620 |
| Leverhulme Trust | United Kingdom | 501100000275 | RPG-2017-362 |
| Ministry of Science and Technology of the People's Republic of China | China | 501100002855 | Unassigned |

Q1

Researcher information

Please check that the researcher information in the table below is correct, including the spelling and formatting of all author names, and that the authors' first, middle and last names have been correctly identified. **Names will be indexed and cited as shown on the proof, so these must be correct.**

If any authors have ORCID or ResearcherID details that are not listed below, please provide these with your proof corrections. Please ensure that the ORCID and ResearcherID details listed below have been assigned to the correct author. Authors should have their own unique ORCID iD and should not use another researcher's, as errors will delay publication.

Please also update your account on our online [manuscript submission system](#) to add your ORCID details, which will then be automatically included in all future submissions. See [here](#) for step-by-step instructions and more information on author identifiers.

| First (given) and middle name(s) | Last (family) name(s) | ResearcherID | ORCID iD |
|----------------------------------|-----------------------|--------------|---------------------|
| Xiaoyan | Tan | | 0000-0002-1742-8252 |
| Emma E. | McCabe | | |
| Fabio | Orlandi | | 0000-0001-6333-521X |
| Pascal | Manuel | | |
| Maria | Batuk | | |
| Joke | Hadermann | | 0000-0002-1756-2566 |

| | | | |
|-------------|-------------|-------------|---------------------|
| Zheng | Deng | | |
| Changqing | Jin | | |
| Israel | Nowik | | |
| Rolfe | Herber | | 0000-0001-5876-9240 |
| Carlo U. | Segre | B-1548-2009 | 0000-0001-7664-1574 |
| Sizhan | Liu | | |
| Mark | Croft | | |
| Chang-Jong | Kang | | 0000-0003-2895-4888 |
| Saul | Lapidus | | |
| Corey E. | Frank | | 0000-0003-2638-7795 |
| Haricharan | Padmanabhan | | |
| Venkatraman | Gopalan | | |
| Meixia | Wu | | |
| Man-Rong | Li | D-1697-2012 | 0000-0001-8424-9134 |
| Gabriel | Kotliar | | |
| David | Walker | | |
| Martha | Greenblatt | | 0000-0002-1806-2766 |

Queries for the attention of the authors

Journal: **Journal of Materials Chemistry C**

Paper: **c8tc05059g**

Title: **MnFe_{0.5}Ru_{0.5}O₃: an above-room-temperature antiferromagnetic semiconductor**

For your information: You can cite this article before you receive notification of the page numbers by using the following format: (authors), J. Mater. Chem. C, (year), DOI: 10.1039/c8tc05059g.

Editor's queries are marked on your proof like this **Q1**, **Q2**, etc. and for your convenience line numbers are indicated like this 5, 10, 15, ...

Please ensure that all queries are answered when returning your proof corrections so that publication of your article is not delayed.

| Query reference | Query | Remarks |
|-----------------|---|---------|
| Q1 | Funder details have been incorporated in the funder table using information provided in the article text. Please check that the funder information in the table is correct. | |
| Q2 | Please confirm that the spelling and format of all author names is correct. Names will be indexed and cited as shown on the proof, so these must be correct. No late corrections can be made. | |
| Q3 | Please check that the Graphical Abstract text fits within the allocated space indicated on the front page of the proof. If the entry does not fit between the two horizontal lines, then please trim the text and/or the title. | |
| Q4 | "Relative" appears to be spelled incorrectly as "Relatvie" in Fig. 10. Please could you supply a corrected version (preferably as a TIF file at 600 dots per inch) with your proof corrections. | |
| Q5 | Please note that a conflict of interest statement is required for all manuscripts. Please read our policy on Conflicts of interest (http://rsc.li/conflicts) and provide a statement with your proof corrections. If no conflicts exist, please state that "There are no conflicts to declare". | |

MnFe_{0.5}Ru_{0.5}O₃: an above-room-temperature
antiferromagnetic semiconductor†

Cite this: DOI: 10.1039/c8tc05059g

Xiaoyan Tan,^a Emma E. McCabe,^b Fabio Orlandi,^c Pascal Manuel,^c Maria Batuk,^d Joke Hadermann,^d Zheng Deng,^e Changqing Jin,^e Israel Nowik,^f Rolfe Herber,^f Carlo U. Segre,^g Sizhan Liu,^h Mark Croft,ⁱ Chang-Jong Kang,ⁱ Saul Lapidus,^j Corey E. Frank,^a Haricharan Padmanabhan,^k Venkatraman Gopalan,^k Meixia Wu,^l Man-Rong Li,^l Gabriel Kotliar,ⁱ David Walker^m and Martha Greenblatt^{a*}

A transition-metal-only MnFe_{0.5}Ru_{0.5}O₃ polycrystalline oxide was prepared by a reaction of starting materials MnO, MnO₂, Fe₂O₃, RuO₂ at 6 GPa and 1873 K for 30 minutes. A combination of X-ray and neutron powder diffraction refinements indicated that MnFe_{0.5}Ru_{0.5}O₃ adopts the corundum (α-Fe₂O₃) structure type with space group *R* $\bar{3}c$, in which all metal ions are disordered. The centrosymmetric nature of the MnFe_{0.5}Ru_{0.5}O₃ structure is corroborated by transmission electron microscopy, lack of optical second harmonic generation, X-ray absorption near edge spectroscopy, and Mössbauer spectroscopy. X-ray absorption near edge spectroscopy of MnFe_{0.5}Ru_{0.5}O₃ showed the oxidation states of Mn, Fe, and Ru to be 2+/3+, 3+, and ~4+, respectively. Resistivity measurements revealed that MnFe_{0.5}Ru_{0.5}O₃ is a semiconductor. Magnetic measurements and magnetic structure refinements indicated that MnFe_{0.5}Ru_{0.5}O₃ orders antiferromagnetically around 400 K, with magnetic moments slightly canted away from the *c* axis. ⁵⁷Fe Mössbauer confirmed the magnetic ordering and Fe³⁺ (*S* = 5/2) magnetic hyperfine splitting. First principles calculations are provided to understand the electronic structure more thoroughly. A comparison of synthesis and properties of MnFe_{0.5}Ru_{0.5}O₃ and related corundum Mn₂BB'O₆ derivatives is discussed.

Received 8th October 2018,
Accepted 12th November 2018

DOI: 10.1039/c8tc05059g

rsc.li/materials-c

Introduction

Spintronics (spin-based electronics or spin transport electronics) is an emergent new technology that takes advantage of the interaction between the charge and magnetic spins of the electrons in materials. Compared to conventional

semiconductor charge-based electronics, devices based on spintronics consume less electric power, provide faster data processing speed and increased storage densities.^{1,2} Promising spintronic materials are ferromagnetic/ferrimagnetic semiconductors (FMS/FiMS) due to the possibility of spin-polarized carriers and facile combination with semiconductor devices.¹

^a Department of Chemistry and Chemical Biology Rutgers, The State University of New Jersey, Piscataway, New Jersey, 08854, USA. E-mail: greenbla@chem.rutgers.edu^b School of Physical Sciences, University of Kent, Canterbury, Kent, CT2 7NH, UK^c ISIS Facility, STFC, Rutherford Appleton Laboratory, Chilton, Didcot, Oxfordshire, OX11 0QX, UK^d EMAT, University of Antwerp, Groenenborgerlaan 171, B-2020 Antwerp, Belgium^e Institute of Physics, School of Physics, University of Chinese Sciences, P. O. Box 603, Beijing, 100190, P. R. China^f Racah Institute of Physics, The Hebrew University, Jerusalem, 91904, Israel^g Department of Physics & CSRRI, Illinois Institute of Technology, Chicago, Illinois, 60616, USA^h Department of Physics, New Jersey Institute of Technology, Newark, New Jersey, 07102, USAⁱ Department of Physics and Astronomy, Rutgers, The State University of New Jersey, Piscataway, New Jersey, 08854, USA^j Advanced Photon Source, Argonne National Laboratory, Argonne, Illinois, 60439, USA^k Department of Materials Science and Engineering, Pennsylvania State University, University Park, Pennsylvania 16802, USA^l Key Laboratory of Bioinorganic and Synthetic Chemistry of Ministry of Education, School of Chemistry, Sun Yat-Sen University, Guangzhou, 510275, P. R. China^m Lamont Doherty Earth Observatory, Columbia University, Palisades, New York, 10964, USA† Electronic supplementary information (ESI) available: Rietveld refinement profiles of synchrotron and neutron data; TGA-DSC measurement; electron diffraction patterns; comparison of the Mn-K and Fe-K edge spectra for MnFe_{0.5}Ru_{0.5}O₃ and α-Fe₂O₃; evolution of the L₃-edges of 4d-row transition metal compounds; ZFC-FC of MnFe_{0.5}Ru_{0.5}O₃ with different applied magnetic field; comparison of magnetic-only Bragg reflections; the intensity of magnetic reflections as a function of temperature; total reflection intensity; coercive field of MnFe_{0.5}Ru_{0.5}O₃ as a function of temperature; and illustration of AFM magnetic structure. See DOI: 10.1039/c8tc05059g

* Present address: Department of Chemistry and Biochemistry, George Mason University, Fairfax, VA, 22030, USA.

1 For practical application, the ideal FMS/FiMS should exhibit
magnetic ordering above room temperature (RT). Designing and
finding such materials is still challenging for scientists in materi-
als science, solid state chemistry, condensed matter physics, and
5 related areas.³ To date, there are few FMS/FiMS materials with an
ordering temperature near or above RT such as spinel
 $\text{Fe}_{0.5}\text{Cu}_{0.5}\text{Cr}_2\text{S}_4$ ($T_C = 340$ K),⁴ perovskite $\text{Sr}_{0.8}\text{Y}_{0.2}\text{CoO}_{3-\delta}$ ($T_C =$
335 K, 310 K for thin films),^{5,6} and double perovskites (DP)
 $\text{La}_2\text{NiMnO}_6$ ($T_C \sim 280$ K) and $\text{Sr}_2\text{CrOsO}_6$ ($T_C \sim 700$ K).⁷⁻⁹

10 Compared to ferromagnets, antiferromagnets are more com-
mon in nature. Recent studies indicate that antiferromagnetic
semiconductors (AFMS) could be alternatives to FMS in spin-
tronics, which motivates further research into the AFM spin-
tronics subfield.¹⁰⁻²⁰ Several near/above RT candidates have
15 been discovered including LiMnAs ($T_N = 374$ K),²¹ CuMnAs
($T_N = 295$ K),^{22,23} FeRh ($T_N \sim 373$ K),²⁴ MnTe ($T_N = 310$ K),²⁵ and
perovskite-type Sr_2IrO_4 ($T_N = 240$ K).^{26,27} However, further
development of the AFM spintronics subfield requires the
discovery of more AFMS with T_N above RT.

20 As mentioned above, DPs are promising spintronic materials
with high magnetic ordering temperatures. In particular, DP and
corundum related oxides, $\text{A}_2\text{BB}'\text{O}_6$, have demonstrated the
required properties. Besides $\text{La}_2\text{NiMnO}_6$ ($T_C \sim 280$ K) and
 $\text{Sr}_2\text{CrOsO}_6$ ($T_C \sim 700$ K),⁷⁻⁹ we recently synthesized several
25 $\text{Mn}_2^{2+}\text{Fe}^{3+}\text{B}^{5+}\text{O}_6$ (B' = Nb, Ta, Mo, Re) phases under high pressure
and temperature, where both the A and B sites are transition
metals.²⁸⁻³⁰ High pressure synthesis of $\text{Mn}_2\text{FeNbO}_6$ and $\text{Mn}_2\text{Fe-}$
 TaO_6 at 1573 K under 7 GPa produced LiNbO_3 (LN)-type polar AFM
insulators with weak FM magnetic ordering around 210 K.²⁸ The
30 magnetic interactions of Mn^{2+} (high spin (HS), d^5) and Fe^{3+} (HS, d^5)
ions (alongside diamagnetic Nb^{5+} and Ta^{5+} ions) are responsible for
magnetic transition temperatures close to RT. The magnetic transi-
tion temperature of $\text{Mn}_2\text{FeB}'\text{O}_6$ are further increased by incorpor-
ating more d^n ($n > 0$) electrons at the B' sites. When Nb^{5+} (d^0) is
35 replaced by Mo^{5+} (d^1), the polar Ni_3TeO_6 (NTO)-type $\text{Mn}_2^{2+}\text{Fe}^{3+}$
 Mo^{5+}O_6 obtained under 8 GPa is an FiMS with $T_C = 337$ K.²⁹ In the
case of $\text{B}'^{5+} = \text{Re}^{5+}$ (d^2), the DP $\text{Mn}_2^{2+}\text{Fe}^{3+}\text{Re}^{5+}\text{O}_6$ formed at 5 GPa
displays giant magnetoresistance as a half-metallic ferrimagnet
with $T_C = 520$ K.³⁰ Following this trend, it was expected that Nb^{5+}
40 (d^0) could also be substituted by Ru^{5+} (d^3) in $\text{MnFe}_{0.5}\text{Ru}_{0.5}\text{O}_3$ for
possible magnetic ordering above RT.

Here, we report that $\text{MnFe}_{0.5}\text{Ru}_{0.5}\text{O}_3$ can be synthesized under
high pressure and high temperature. The crystal structure, formal
oxidation states of cations, magnetic and electrical properties have
45 been investigated. Neutron diffraction and Mössbauer spectro-
scopy data were also measured to elucidate the magnetic ordering
in the structure. First principles calculations were undertaken to
understand the electronic structure more thoroughly. Good agree-
ment is found between the experiments and the DFT calculations.

50

Experimental section

Starting materials and synthesis

55 Polycrystalline $\text{MnFe}_{0.5}\text{Ru}_{0.5}\text{O}_3$ was prepared by high-pressure
and high-temperature synthesis with a Walker-type Multi-Anvil

press as described in our previous work.²⁸⁻³¹ A stoichiometric
mixture of MnO (wt 99.99%, Alfa Aesar), MnO_2 (wt 99.99%,
Alfa Aesar), Fe_2O_3 (wt 99.999%, Sigma Aldrich) and RuO_2 (wt
99.9%, Alfa Aesar) was first ground well at ambient pressure.
The oxide mixture was then packed into a Pt capsule inside a
5 MgO crucible, which was later assembled with other parts of
the high-pressure apparatus. The reaction was carried out at
1873 K under 6 GPa for 0.5 h and then quenched to room
temperature in a few minutes. After quenching, the pressure
was slowly released. The resulting sample was a black pellet,
10 with a total mass of ~ 25 mg. To make enough sample (~ 100
mg) for neutron experiment, four experiments were carried out
with the same synthetic conditions, and the resulting samples
were checked by X-ray powder diffraction (XRPD).

Chemical analysis

The chemical composition of the samples was determined by
energy dispersive X-ray (EDX) analysis conducted on a JEOL
5510 scanning electron microscope equipped with an INCAX-
sight 6587 system (Oxford Instruments). Mn-K, Fe-K and Ru-L
20 lines were used for the composition quantification.

Thermogravimetric analysis (TGA) and differential scanning calorimetry (DSC)

A powder sample of about 30 mg was loaded into an alumina
crucible and measured in an SDT Q600 TA Instrument. The
sample was tested from room temperature to 1000 °C at a
heating and cooling rate of 10 °C min^{-1} under Ar flow. The
remaining powder after the measurement was analyzed
by XRPD.

X-ray powder diffraction (XRPD)

Samples were measured in the 2θ range from 10° to 80° and
collected for 1 h on a Bruker D8 Advance Diffractometer (Cu $K\alpha$,
 $\lambda = 1.5418$ Å) with a SOL-X solid state detector. RT synchrotron
35 powder X-ray diffraction ($\lambda = 0.4126$ Å) was collected in the 2θ
range from 0.5° to 50° at the 11-BM beam line at the Advanced
Photon Source (APS) of Argonne National Laboratory. High-
resolution powder X-ray diffraction data were also collected at
room temperature on a Rigaku SmartLab X-ray diffractometer
40 using a Ge220 monochromator to select the Cu $K\alpha$, $\lambda = 1.5418$ Å
wavelength.

Neutron powder diffraction (NPD)

NPD data were collected on ~ 100 mg $\text{MnFe}_{0.5}\text{Ru}_{0.5}\text{O}_3$ powder
sample placed inside a 3 mm diameter thin-walled cylindrical
vanadium can at the ISIS neutron and muon source (Ruther-
ford Appleton Laboratory, U.K.) on the WISH diffractometer
located in the second target station.³² Multibank (153°, 122°,
90°, 58°, 27°) data were collected at 450 K (~ 30 minutes) and
50 the sample was then cooled to 5 K in a closed-cycle refrigerator
(CCR) and a high quality dataset (~ 2 hours) was recorded.
Shorter scans were then collected on warming (~ 15 minutes
scans in 20 K increments to 75 K, and then at 25 K increments
55 to 300 K, with longer 60 minutes scans collected at 60 and 125
K). Rietveld refinements were carried out with Topas

1 Academic^{33,34} and the magnetic symmetry analysis was carried out with ISODISTORT.³⁵

Transmission electron microscopy (TEM)

5 The samples for TEM analysis were prepared by mixing the powders with ethanol in an ultrasonic bath and depositing a few drops of the obtained suspension onto a holey TEM grid covered with carbon. Electron diffraction (ED) patterns were acquired with a Phillips CM20 microscope operated at 200 kV. High angle annular dark field (HAADF) scanning transmission electron microscopy (STEM) images were acquired with a FEI Titan 80-300 “cubed” microscope operated at 300 kV. The simulated HAADF-STEM images were calculated with the QSTEM software.³⁶

Second harmonic generation (SHG)

20 The measurements were done in far-field reflection geometry at normal incidence inside a cryostat. A pulsed laser beam from a Ti:sapphire femtosecond laser with a wavelength of 800 nm (pulse width 80 fs, repetition rate 80 MHz) was focused on a polished polycrystalline pellet sample with a 50× objective onto a spot size of 0.5 μm. The reflected light was passed through a filter to eliminate the 800 nm fundamental, and then collected with a photomultiplier tube to detect any signal at the second harmonic of 400 nm.

X-ray absorption near edge spectroscopy (XANES)

30 XANES was carried out to confirm the formal oxidation state of the cations in MnFe_{0.5}Ru_{0.5}O₃. Mn, Fe and Ru K-edge data were collected at the 10-ID and 11-ID beam line at the APS of Argonne National Laboratory and the 8-ID ISS beamline at the National Synchrotron Light Source II (NSLS-II), at Brookhaven National Laboratory. The Ru L_{2,3}-edge measurements were performed at the NSLS-II TES, 8-BM beamline. Standard spectra collected previously at X19A at (NSLS-I) are also included over most of the energy ranges.

Magnetic measurements

40 Magnetic properties were measured on polycrystalline sample with a Quantum Design SQUID MPMS-XL magnetometer. Field-cooled (FC) and zero-field-cooled (ZFC) magnetizations were measured between 1.8 and 300 K in a direct-current applied field. Field dependence of isothermal magnetization was measured with the applied field varying from −6 to 6 T.

Mössbauer spectroscopy

50 The ⁵⁷Fe Mössbauer studies were performed with a conventional constant acceleration drive in transmission mode, in conjunction with a 50 mCi ⁵⁷Co:Rh source. The absorber, MnFe_{0.5}Ru_{0.5}O₃, was crushed to fine powder and put into a Perspex absorber holder. Measurements were performed while the absorber was in a cryostat with temperature stabilization (to 0.5°) in the range of 90 to 400 K. The obtained spectra were analyzed, in terms of a least square fit procedure, to simulated model spectra.

Electrical resistivity

Resistivity measurements were conducted with a Quantum Design Physical Property Measurement System (PPMS) with standard four-probe technique.

DFT calculations

Density functional theory (DFT) was used to investigate the type of crystal structure and magnetic order that give stable phases, to confirm the experimental findings. To treat the structural disorder observed in the experiments, the virtual crystal approximation (VCA) method³⁷ implemented in Quantum Espresso code^{38,39} was employed within the Vanderbilt ultra-soft-pseudopotential scheme.⁴⁰ The kinetic energy cutoffs for wave functions and charge density were set to be 50 and 400 Ry, respectively in the VCA calculations. After the stable crystal structure was found through the VCA calculations, the electronic structures have been studied with two different magnetic structures (antiferro- and ferro-magnetic ordering) using the full-potential linearized augmented plane-wave method implemented in WIEN2k.⁴¹ In the magnetic calculations, the structural disorder was ignored and the Fe occupancy was regarded to be 100% at the disordered sites for simplicity. Generalized gradient approximation (GGA) of Perdew–Burke–Ernzerhof (PBE)⁴² was used for the exchange–correlation functional and 25 × 25 × 7 *k* points were used for the Brillouin zone sampling. To obtain the correct ground state (including the magnetic moment of Fe³⁺ and an insulating phase), GGA+*U* was adopted within fully localized limit.^{43,44} The effective on-site Coulomb interaction parameter $U_{\text{eff}} = U - J = 4$ eV was used.

Results and discussion

Crystal structure and thermal stability

35 Similar to the synthesis of Mn₂FeMo₆ (M = Nb, Ta, Mo, W, Re), MnFe_{0.5}Ru_{0.5}O₃ was prepared at 1873 K under 6 GPa with a Walker-type Multi-Anvil press. Incident illumination, plane-polarized optical micrographs shows the target phase with ~100 μm grain size, and trace of RuO₂ and FeMnO_x impurities (Fig. S2, ESI†). The XRPD pattern (Fig. S2, ESI†) indicates either a disordered α-Fe₂O₃-type (Fig. 1a, corundum, *R*3̄*c*) or LN-type

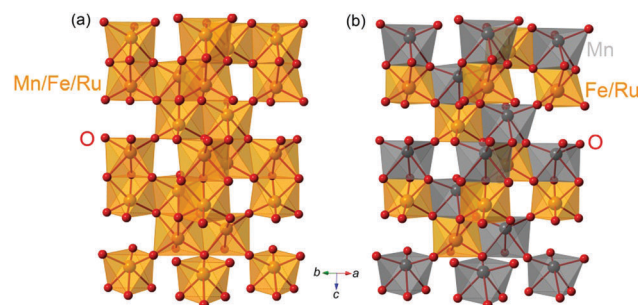


Fig. 1 Crystal structures of MnFe_{0.5}Ru_{0.5}O₃ with α-Fe₂O₃ type (a, corundum, *R*3̄*c*), and LN-type (b, *R*3̄*c*) viewed along the [110] direction. Color code: (Mn/Fe/Ru)O₆ = orange in (a), MnO₆/(Fe/Ru)O₆ = gray/orange in (b), O = red spheres.

(Fig. 1b, $R3c$) as the main phase with a small amount RuO_2 impurity (\sim wt 2%). Both structures give the same allowed reflections in diffraction experiments due to Friedel's law.

Both corundum and LN crystal structures have the same 3-dimensional (3D) construction based on distorted MO_6 ($M = \text{Mn}, \text{Fe}, \text{ or Ru}$) octahedra. The centrosymmetric corundum crystal structure consists of symmetric dimers of MO_6 octahedra connected *via* face-sharing along the $[001]$ direction and edge-sharing in (001) planes. All metal sites are disordered, and each MO_6 ($M = \text{Mn/Fe/Ru}$) is distorted with M cations displaced from the centers of octahedra, resulting in three long and three short $M\text{--O}$ bond distances (Fig. 1a). The cation-ordered non-centrosymmetric LN structure is derived from this corundum structure, but with two cation sites, allowing ordering of Mn, Fe and Ru over these sites (*e.g.* a Mn site, and a mixed Fe/Ru site). This would give a LN model with distorted dimers of MnO_6 and MO_6 ($M = \text{Fe}, \text{ Ru}$) octahedra face-sharing along $[001]$ (Fig. 1b). Besides LN, other corundum derivatives are centrosymmetric ilmenite ($\text{IL}, R\bar{3}$), noncentrosymmetric ordered ilmenite ($\text{OIL}, R3$), and NTO ($R3$), which have the same 3D network of MO_6 octahedra but with different cation arrangements.⁴⁵

The chemical composition of $\text{MnFe}_{0.5}\text{Ru}_{0.5}\text{O}_3$ was confirmed by EDX with the formula $\text{Mn}_{2.01(8)}\text{Fe}_{1.00(6)}\text{Ru}_{1.00(12)}\text{O}_x$ and the thermal stability of this sample was measured by TGA-DSC. Above 800°C , the sample starts decomposing into MnFe_2O_4 , or FeMn_2O_4 and RuO_2 (Fig. S3, ESI[†]).

X-ray and neutron powder diffraction

Because Rietveld refinements with XRPD data gave similar fits to corundum ($R3c$) or LN-type ($R3c$) structure (Fig. S2, ESI[†]), and Fe and Mn are indistinguishable to Cu $K\alpha$ radiation, RT XRPD data were used to determine only the distribution of Ru over the two cation sites in the LN model. Refinements suggested a statistical distribution of Ru over the two sites, with Ru occupancies of 0.27(2) at $(0\ 0\ z)$, and 0.23(2) at $(0\ 0\ 0)$, respectively. The R_{wp} from this model is 7.12%, which is slightly smaller than that (7.15%) of a disordered LN model with Ru occupancies of 0.25 on both sites (Fig. S4 and Tables S1, S2, ESI[†]) analogous to the corundum model due to cation disorder. Therefore, a statistical distribution of Ru seems most likely in $\text{MnFe}_{0.5}\text{Ru}_{0.5}\text{O}_3$ based on XRPD data analysis.

The Ru distribution was then fixed (Ru occupancies of 0.25 on both sites) in a starting LN model for multibank refinement using 450 K NPD data to refine the distribution of Fe and Mn over the two sites. NPD is expected to be very sensitive to this distribution, given the strong contrast in neutron scattering lengths ($\text{Mn} = -3.73\text{ fm}$, $\text{Fe} = 9.54\text{ fm}$, $\text{Ru} = 7.21\text{ fm}$).⁴⁶ A fully disordered LN model (analogous to corundum) gave a good fit to the data ($R_{\text{wp}} = 3.192\%$). Allowing the Fe and Mn distribution to refine resulted in a marginal improvement in fit ($R_{\text{wp}} = 3.179\%$) but suggested an almost statistical distribution of Fe and Mn over the two sites, Ru/Fe/Mn occupancy of 0.25/0.227(3)/0.523(3) at $(0\ 0\ z)$, and 0.25/0.275(3)/0.477(3) at $(0\ 0\ 0)$ (Fig. S5 and Table S3, ESI[†]). This analysis suggests that a fully disordered corundum model is most appropriate to describe the crystal structure of $\text{MnFe}_{0.5}\text{Ru}_{0.5}\text{O}_3$, at least at the length scale probed by diffraction techniques.

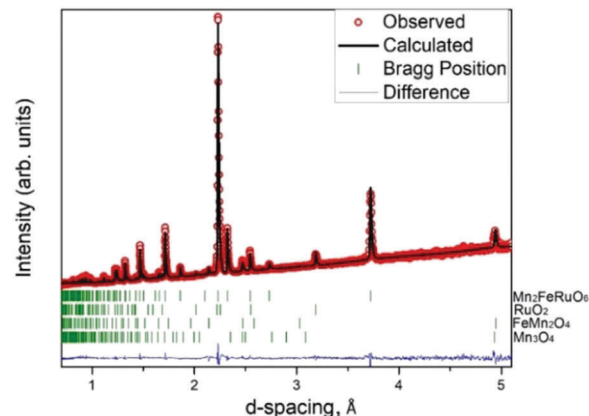


Fig. 2 Refinement profiles for $\text{MnFe}_{0.5}\text{Ru}_{0.5}\text{O}_3$ in corundum ($R\bar{3}c$) model, using 450 K NPD 122° bank data. Observed, calculated, Bragg position, and difference profiles are shown in red, black, green, and blue, respectively.

Table 1 Refinement details of corundum ($R\bar{3}c$) model of $\text{MnFe}_{0.5}\text{Ru}_{0.5}\text{O}_3$ using 450 K NPD data with $a = 5.0870(1)\text{ \AA}$, $c = 13.9306(3)\text{ \AA}$; $R_{\text{wp}} = 3.19\%$, $R_p = 3.04\%$ and $\chi^2 = 2.27$

| Atom | Site | x | y | z | Fractional occupancy | $U_{\text{iso}} \times 100 (\text{\AA}^2)$ |
|----------|------|-----------|-----|-----------|----------------------|--|
| Mn/Ru/Fe | 12c | 0 | 0 | 0.3497(1) | 0.5/0.25/0.25 | 2.55(9) |
| O | 18e | 0.3073(1) | 0 | 0.25 | 1 | 2.54(7) |

Table 2 Selected bond lengths and angles from Rietveld refinement of corundum ($R\bar{3}c$) model of $\text{MnFe}_{0.5}\text{Ru}_{0.5}\text{O}_3$ using 450 K NPD data

| Bond | Length (\AA) | Angle ($^\circ$) | |
|------|-------------------------|-------------------------------------|----------|
| M–O | $3 \times 1.997(1)$ | M–O(1)–M (within open face) | 99.93(5) |
| M–O | $3 \times 2.090(1)$ | M–O(1)–M (from open to shared face) | 91.01(1) |
| M–M | $1 \times 2.777(3)$ | M–O(1)–M (within shared face) | 80.71(5) |

The disordered corundum model was then used for multi-bank (153° , 122° , 90° , 58° , 27° banks of data) Rietveld refinement of 450 K NPD data, and the results are shown in Fig. 2 (122° bank data fit profile), Tables 1, 2, and Fig. S6 (ESI[†]) (all bank data fit profiles). Several small impurity phases were also included in the refinements, including RuO_2 (wt 3.2(1)%), FeMn_2O_4 (wt 2.1(1)%) and Mn_3O_4 (wt 4(1)%).

The refined unit cell parameters are $a = 5.0870(1)\text{ \AA}$, $c = 13.9306(3)\text{ \AA}$, $V = 360.5(8)\text{ \AA}^3$ (Table 1). The unit cell parameter a of $\text{MnFe}_{0.5}\text{Ru}_{0.5}\text{O}_3$ is much smaller than those of LN-type Mn_2FeMO_6 ($M = \text{Nb}, \text{ Ta}$, $a \sim 5.27\text{ \AA}$), while the c -axis is slightly larger than that of $\text{Mn}_2\text{FeTaO}_6$ ($c = 13.8892(3)\text{ \AA}$), but smaller than that of $\text{Mn}_2\text{FeNbO}_6$ ($c = 13.9338(2)\text{ \AA}$). The average M–O bond lengths are about 2.05 \AA (Table 2), which is much shorter than those of Mn–O in $\text{Mn}_2^{2+}\text{Fe}^{3+}\text{NbO}_6$ (2.16 \AA) and $\text{Mn}_2^{2+}\text{Fe}^{3+}\text{TaO}_6$ (2.22 \AA). These values are also smaller than those ($\sim 2.2\text{ \AA}$) in other corundum derivative analogs such as $\text{Mn}_2^{2+}\text{Fe}^{3+}\text{M}^{5+}\text{O}_6$ ($M = \text{Mo}, \text{ Sb}$) and $\text{Mn}_2^{2+}\text{Fe}^{2+}\text{W}^{6+}\text{O}_6$. The M–O bond length analysis indicates that Mn is likely not purely Mn^{2+} in the structure. The average M–O bond length ($\sim 2.05\text{ \AA}$) is comparable with those in $\text{Mn}_2^{2+}\text{Fe}^{3+}\text{Nb}^{5+}\text{O}_6$ (2.035 \AA), $\text{Mn}_2^{2+}\text{Fe}^{3+}\text{Ta}^{5+}\text{O}_6$

(2.01 Å), $\text{Mn}_2^{2+}\text{Fe}^{3+}\text{Mo}^{5+}\text{O}_6$ (2.033 Å), and $\text{Mn}_2^{2+}\text{Fe}^{3+}\text{Sb}^{5+}\text{O}_6$ (2.006 Å). However, they are shorter than those in $\text{Mn}_2^{2+}\text{Fe}^{2+}\text{W}^{6+}\text{O}_6$ (2.154 Å), which support Fe^{3+} in $\text{MnFe}_{0.5}\text{Ru}_{0.5}\text{O}_3$. The detailed cation oxidation states will be discussed in the XANES results.

Transmission electron microscopy

To distinguish between LN-type $R3c$ and corundum $R\bar{3}c$ models for $\text{MnFe}_{0.5}\text{Ru}_{0.5}\text{O}_3$, as shown in Fig. 1, TEM experiments were also carried out. Electron diffraction patterns of $\text{MnFe}_{0.5}\text{Ru}_{0.5}\text{O}_3$ are shown in Fig. 3 and Fig. S7 (ESI[†]), respectively. The patterns agree with the reflection conditions of the $R3c$ and $R\bar{3}c$ space groups: hkl : $-h+k+l=3n$; $hk0$: $-h+k=3n$; $h\bar{h}l$: $h+l=3n$, $l=2n$; hhl : $l=3n$; $00l$: $l=6n$. In Fig. S6 (ESI[†]), reflection $0\bar{1}1$ and its symmetrically equivalent reflections in the $[211]$ zone and $00l$: $l=3n$ in the $[210]$ zone are due to double diffraction. Based only on selected area ED patterns, it is impossible to distinguish between $R3c$ and $R\bar{3}c$ space groups. Therefore, we tested the models for the two space groups against experimental HAADF-STEM images.

In the LN $R3c$ models, there are distinct columns of A and B/B' sites of different stoichiometry, while in the corundum $R\bar{3}c$ model, all three atomic species are intermixed. There are two projections that allow separate visualization of the A and B/B' columns in the $R3c$ structure: $[100]$ and $[2\bar{2}1]$. On HAADF-STEM images, the brightness of the dots is proportional to the average atomic number of the projected column: $I \sim Z^2$. In $\text{MnFe}_{0.5}\text{Ru}_{0.5}\text{O}_3$, $Z_{\text{Mn}} = 25$, $Z_{\text{Fe}} = 26$, $Z_{\text{Ru}} = 44$ and therefore in case of ordering, columns with on average heavier cations should appear brighter.

HAADF-STEM images were taken along both those $[100]$ and $[2\bar{2}1]$ directions (Fig. 3c and d). There is no systematic

difference in the intensity of the different atomic columns. The ratio between the summed intensity of A and B/B' sites, from profiles of 10 different rows of either A or B/B', is very close to 1. Moreover, intensity profiles for ten rows with pairs of A and B/B' columns (Fig. S8, ESI[†]) do not show any systematic difference in the intensities. The differences between the A and B/B' peaks are random and can be explained by a statistical difference in the occupation of one column to the next. Therefore, there is no ordering between Mn, Fe and Ru cations in $\text{MnFe}_{0.5}\text{Ru}_{0.5}\text{O}_3$ and the results agree with an $R\bar{3}c$ (and not an $R3c$) model, which is consistent with the results from XRPD and NPD analysis above, and with the disorder suggested by SHG, XANES and Mössbauer data below.

Second harmonic generation

SHG is a sensitive probe of inversion symmetry breaking in single crystal and polycrystalline materials. The SHG response of polycrystalline $\text{MnFe}_{0.5}\text{Ru}_{0.5}\text{O}_3$ was probed with SHG microscopy. Similar techniques have been used by the authors in the past to study inversion symmetry breaking in single crystal and polycrystalline complex oxides.⁴⁷ Measurements were carried out at 300 and 25 K. There is no SHG signal above the background noise level at either temperature, which indicates that the material is centrosymmetric in this temperature range.

X-ray absorption near edge spectroscopy

XANES measurements were performed to probe the Mn, Fe, Ru oxidation state in $\text{MnFe}_{0.5}\text{Ru}_{0.5}\text{O}_3$. The Fe-K main-edge in $\text{MnFe}_{0.5}\text{Ru}_{0.5}\text{O}_3$ appears to correspond to $\sim\text{Fe}^{3+}$ with somewhat broad main edge features bearing some similarity to the LN structure standard spectra for Mn_2FeMO_6 ($M = \text{Ta}$ and Nb) (Fig. 4).

Interestingly, compared to Mn_2FeMO_6 spectra, the $\text{MnFe}_{0.5}\text{Ru}_{0.5}\text{O}_3$ spectrum manifests two features, an additional shoulder on the initial rising portion of the main edge (labeled "1" in Fig. 4a), and a prominent absolute-peak shifted to higher energy (labeled "2" in Fig. 4a). These two features are however present (albeit being more sharply defined) in the corundum ($\alpha\text{-Fe}_2\text{O}_3$) standard spectrum. Thus, the Fe-K main-edge appears to support a corundum ($\alpha\text{-Fe}_2\text{O}_3$) structure for $\text{MnFe}_{0.5}\text{Ru}_{0.5}\text{O}_3$.

The Mn-K main-edge in $\text{MnFe}_{0.5}\text{Ru}_{0.5}\text{O}_3$ is dramatically different from those of the LN structure standard spectra for Mn_2FeMO_6 ($M = \text{Ta}$ and Nb) (Fig. 5), thereby precluding a Mn^{2+} , LN structure in this compound. In terms of chemical shift, the Mn-K main edge appears to be consistent with a substantial Mn^{3+} component, which is similar to that of its Fe-K edge in Fig. 4a. A comparison of the near-edge and post-edge fine structure features (Fig. S9, ESI[†]) emphasize the similar features over the entire energy range, which suggests that the Mn and Fe sites in $\text{MnFe}_{0.5}\text{Ru}_{0.5}\text{O}_3$ are the same and are essentially the same as that in the corundum $\alpha\text{-Fe}_2\text{O}_3$ compound. The notably larger shoulder (on the leading main-edge rise), and decreased intensity in the peak-region of spectrum (relative to the shifted Fe spectrum) indicates a greater admixture of Mn^{2+} character at the Mn sites.

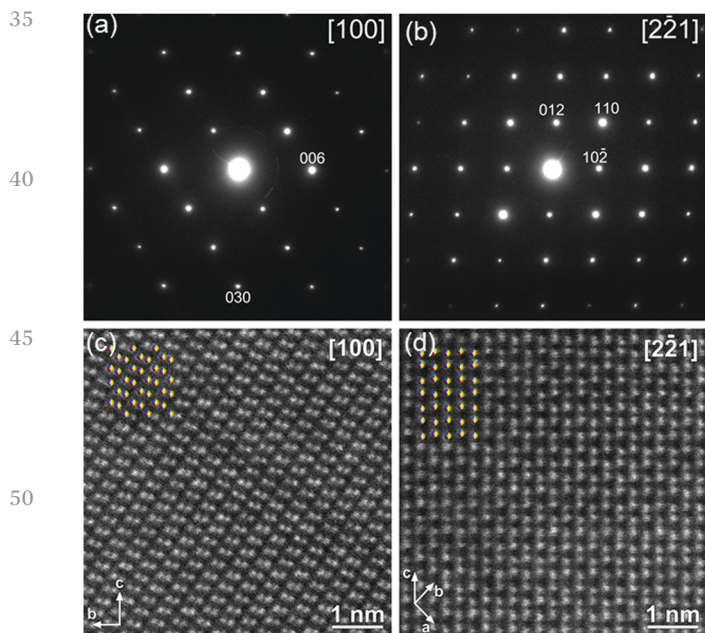


Fig. 3 Electron diffraction patterns (a and b) and HAADF-STEM images (c and d) of $\text{MnFe}_{0.5}\text{Ru}_{0.5}\text{O}_3$ along $[100]$ and $[2\bar{2}1]$ directions.

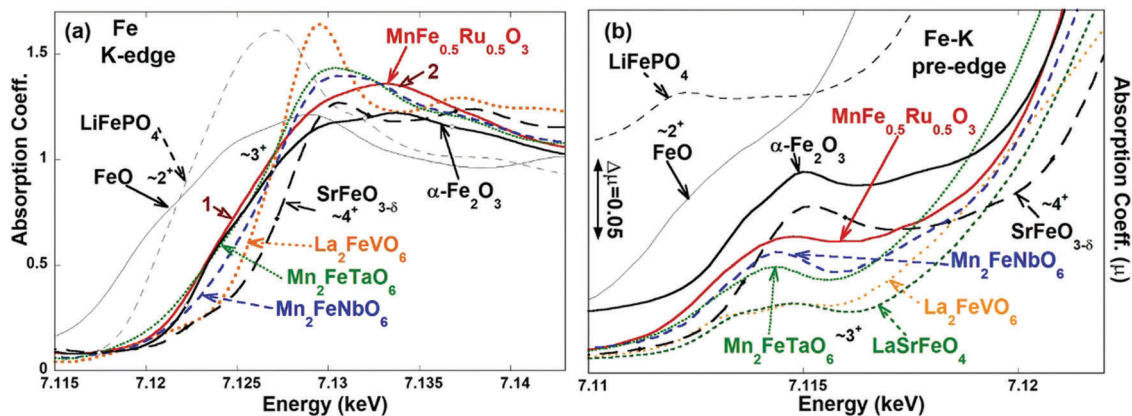


Fig. 4 The Fe-K main-edge (a) and pre-edge (b) spectra for $\text{MnFe}_{0.5}\text{Ru}_{0.5}\text{O}_3$ and other Fe compounds with varying formal valences: the $\sim 2+$ standards FeO and LiFePO_4 ; the $\sim 3+$ perovskite standard La_2FeVO_6 , the $\sim 3+$ corundum $\alpha\text{-Fe}_2\text{O}_3$, and the $\sim 3+$ LiNbO_3 -type standards Mn_2FeMO_6 ($M = \text{Ta}$ and Nb); and the $\sim 4+$ standard SrFeO_3 , all of which have octahedral Fe–O coordination.

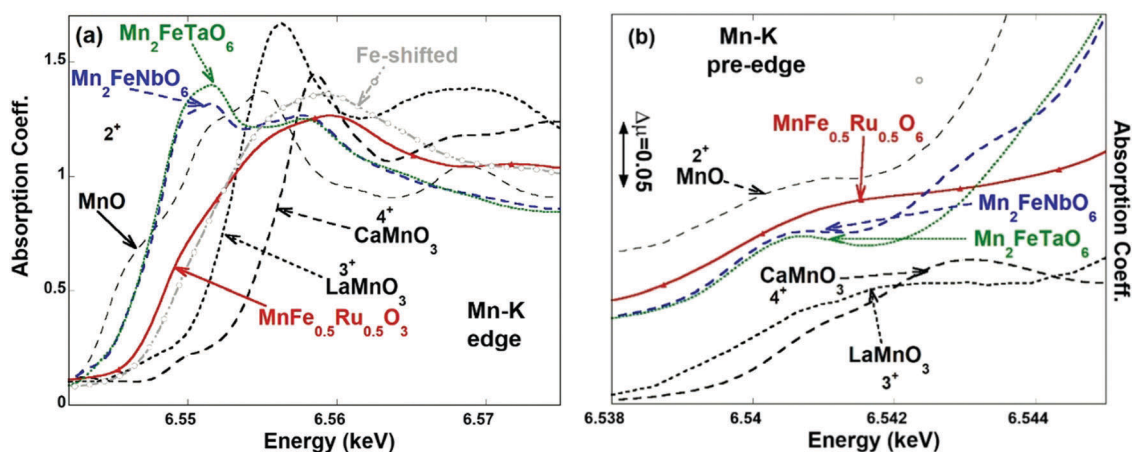


Fig. 5 The Mn-K main edge (a) and pre-edge spectra (b) for $\text{MnFe}_{0.5}\text{Ru}_{0.5}\text{O}_3$ and other Mn compounds with varying formal valences: the $\sim 2+$ standards MnO , the LN structure Mn_2FeMO_6 ($M = \text{Ta}$ and Nb) standards; the perovskite based $\sim 3+$ LaMnO_3 ; and $\sim 4+$ CaMnO_3 standards. Note the Fe-shifted curve in which the Fe-K edge for the compound (from Fig. 4a) has been shifted down energy by 0.57397 keV, the difference in the peak energies of MnO and FeO .

The Mn-K pre-edge of $\text{MnFe}_{0.5}\text{Ru}_{0.5}\text{O}_3$ is substantially broadened compared to the pre-edges of the LN structure standards (Fig. 5b). Moreover, the pre-edges of the LN structures standards are significantly different from the $\text{MnFe}_{0.5}\text{Ru}_{0.5}\text{O}_3$ pre-edge, yet again arguing for a corundum structure and against a LN structure.

Based on the chemical shift of the Ru-K edge as compared with Ru and RuO_2 standards (Fig. 6a), the Ru valence state is close-to, or somewhat-less-than the Ru^{4+} state in RuO_2 . The $L_{2,3}$ -edges of 4d transition metals are sensitive to the electron configuration both through the chemical shift and the structure of the intense near edge “white line” (WL) features.^{48–54} The chemical shift of the Ru- $L_{2,3}$ edge spectra in $\text{MnFe}_{0.5}\text{Ru}_{0.5}\text{O}_3$, compared to the Sr_2YRuO_6 (Ru^{5+} , d^3), and Y_2CoRuO_6 (Ru^{4+} , d^4) standards (Fig. 6b), are clearly consistent with a $\sim d^4$ Ru^{+4} configuration. The intense WL-features at the $L_{2,3}$ edges of 4d transition metal sites in compounds with octahedral O-ligand coordination manifest a distinctly bimodal A/B feature structure due to transitions into empty t_{2g}/e_g d-states. The filling of the t_{2g} -states with increasing d-electron count is reflected

in the $L_{2,3}$ edge spectra by a systematic decrease in the A-feature intensity (relative to the B-feature) as illustrated in Fig. S10 (ESI[†]) for L_3 edge spectra for a series of d^0 to d^4 compounds.

In Fig. 6b, the dramatic decrease in relative A-feature intensity between the Sr_2YRuO_6 (Ru^{5+} , d^3) and Y_2CoRuO_6 (Ru^{4+} , d^4) standards should be noted. For the $\text{MnFe}_{0.5}\text{Ru}_{0.5}\text{O}_3$ $L_{2,3}$ edge spectra, the A-feature intensity appears as an unresolved shoulder on the B-feature. In view of the multiple local environments in the Mn/Fe/Ru site distribution, the inhomogeneity broadening of the ligand field splitting (and the A/B-feature) is reasonable. The amplitude of the A-feature is consistent with a $\sim d^4$ Ru^{4+} configuration. Therefore, both the spectral chemical shift and WLA/B-feature are suggestive of a somewhat reduced Ru^{4+} valence. These observations are consistent with the Fe^{3+} and mixed $\text{Mn}^{2+/3+}$ suggested by XANES results.

Magnetic properties

FC and ZFC magnetic susceptibilities of polycrystalline samples indicate a transition around 375 K (Fig. 7). As the temperature

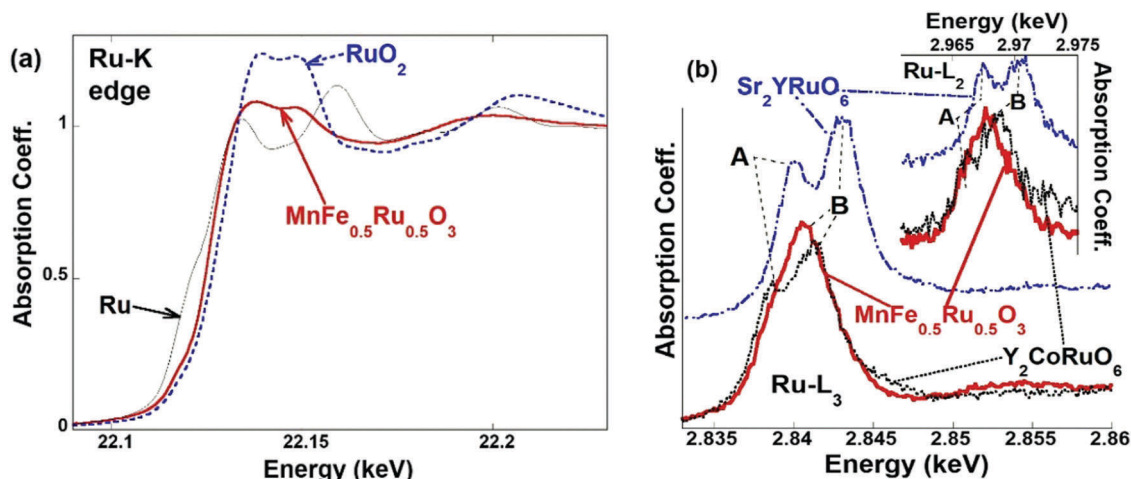


Fig. 6 (a) A comparison of the Ru-K edge spectra for $\text{MnFe}_{0.5}\text{Ru}_{0.5}\text{O}_3$ to the Ru and RuO_2 standards. (b) A comparison of the Ru-L₃ edge spectra for $\text{MnFe}_{0.5}\text{Ru}_{0.5}\text{O}_3$ to the Sr_2YRuO_6 and Y_2CoRuO_6 standards (lower left) along with the Ru-L₂ edge spectra for the same compounds (inset upper right). Note the A- and B-features related respectively to transitions into empty t_{2g} and e_g final states.

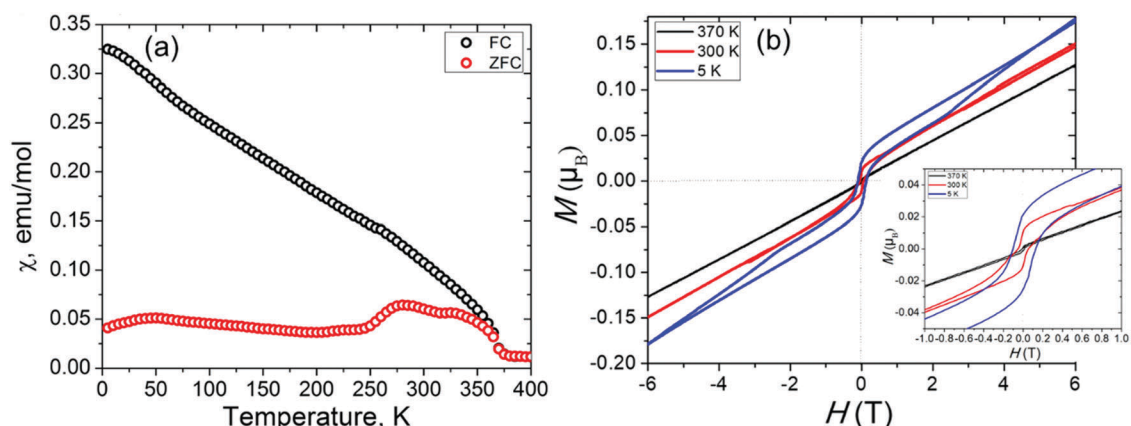


Fig. 7 (a) FC and ZFC magnetic susceptibilities of $\text{MnFe}_{0.5}\text{Ru}_{0.5}\text{O}_3$ as a function of temperature with the applied magnetic field of 0.1 T. (b) Isothermal magnetization as a function of field measured at 5, 300, 370 K. Inset in (b) shows the magnetization between -1 and 1 T.

decreases, the FC magnetic susceptibility keeps increasing, and two slight transitions occur near 80 and 45 K, respectively. These two transitions are more obvious when the sample is measured with lower magnetic field (Fig. S11, ESI[†]). The observed divergence between ZFC-FC curves is due to the anisotropy in the sample, which decreases as the magnetic field increases (Fig. S11, ESI[†]).

Based on the above NPD analysis, the sample contains a small amount of FeMn_2O_4 ($T_C = 373$, 50 K),⁵⁵ and Mn_3O_4 ($T_N = 42$ K)⁵⁶ impurities. Temperature dependent NPD (Fig. 9) indicates that the sample orders AFM around 400 K. There are no additional magnetic transitions; no additional reflections or changes in the temperature behavior of the magnetic Bragg peaks were observed below 80 K, Fig. S12 (ESI[†]). Therefore, the high transition temperature near 375 K may stem from both the sample and possible impurity FeMn_2O_4 or isostructural $\text{Fe}_{1+x}\text{Mn}_{2-x}\text{O}_4$ ($0 < x < 1$). The small low temperature transitions can be attributed to impurities $\text{Fe}_{1+x}\text{Mn}_{2-x}\text{O}_4$ and Mn_3O_4 . The above RT magnetic transition feature is

reminiscent of those of $\text{Mn}_2\text{FeMoO}_6$ ($T_C = 337$ K),²⁹ and $\text{Mn}_2\text{FeReO}_6$ ($T_C = 520$ K).³⁰

The isothermal magnetization measured at 370 K (Fig. 7b) shows almost linear behavior above 50 Oe, and there is almost no hysteresis at this temperature. However, the magnetization measured at 300 and 5 K increased more abruptly at low field (below 2000 Oe) and hysteresis loops were observed at both temperatures. As the temperature decreases, the hysteresis loops enlarge, with larger remnant magnetization and coercivity (Fig. S13, ESI[†]). The overall maximum moment at 6 T is very small, which confirms the AFM ordering and possible FiM ordering from impurity $\text{Fe}_x\text{Mn}_{3-x}\text{O}_4$.

Magnetic structure

To understand the nature of the magnetic ordering, neutron diffraction data were recorded from 5 to 450 K. Compared to the data collected at 450 K, additional magnetic Bragg reflections 021 at ~ 2.2 Å, 101 at ~ 4.2 Å, and 003 at ~ 3.6 Å were observed in NPD data collected at 5 K (Fig. 8 and Fig. S12, ESI[†]).

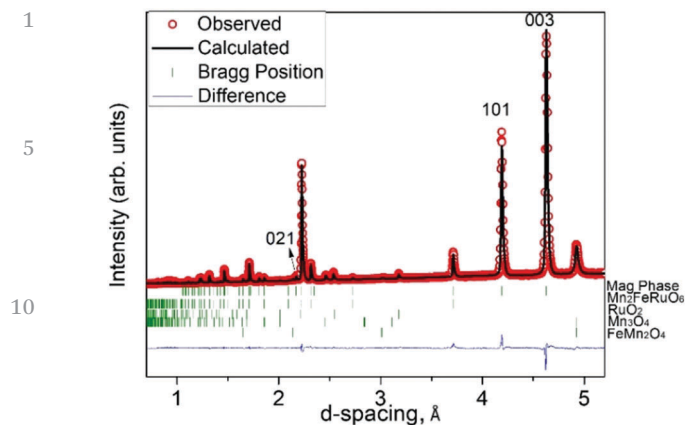


Fig. 8 NPD refinement profiles for $\text{MnFe}_{0.5}\text{Ru}_{0.5}\text{O}_3$ in corundum ($R\bar{3}c$) model at 5 K (122° bank data). Observed, calculated and difference profiles are shown in red, black and blue, respectively. Green ticks show reflection positions for the magnetic ordering in $\text{MnFe}_{0.5}\text{Ru}_{0.5}\text{O}_3$, RuO_2 , Mn_3O_4 , and FeMn_2O_4 Pawley phase in order.

These were indexed by a magnetic unit cell with the same dimensions as the nuclear unit cell. Magnetic intensity is observed for $00l$ reflections, indicating a significant component of the moments within the ab plane.

ISODISTORT³⁵ was used to explore possible magnetic structures (Table S6, ESI†), and those with $m\Gamma_3$ modes predicted some intensity in the positions of the magnetic Bragg reflections. The data is best fit with the cation disordered ($R\bar{3}c$) nuclear structure and a $P\bar{1}$ magnetic unit cell (Fig. S14, $a_{\text{mag}} = b_{\text{mag}}a_n$; $c_{\text{mag}} \approx 5.48 \text{ \AA}$; $\alpha_{\text{mag}} = \beta_{\text{mag}} \approx 62.4^\circ$; $\gamma_{\text{mag}} = 60^\circ$, ESI†) with magnetic moments in-plane described $m\Gamma_{3+}$ modes, and an additional out-of-plane (AFM) component described by a $m\Gamma_{1+}$ mode. This low symmetry magnetic model allows four independent in-plane magnetic $m\Gamma_{3+}$ modes that are highly correlated in analysis using powder diffraction data, since powder data are not sensitive to the in-plane spin direction.

The best fit was obtained with $P\bar{1}$ magnetic model, with two in-plane $m\Gamma_{3+}$ modes (with constraints to give modes of opposite sign) and one mode ($m\Gamma_{3+} \times E^* 2(a)$) constrained to be $1/\sqrt{2}$ in magnitude smaller than the other ($m\Gamma_{3+} \times E^* 1(a)$). This gives a collinear AFM magnetic model with moments antiparallel and oriented along $[120]$. This constrained model gives an equivalent fit to the unconstrained model (R_{wp} values for the two models are identical to two decimal places), and gives equal moments on each site as expected for this cation-disordered semiconducting oxide (and avoids high levels of correlation for the unconstrained models). The fit is improved noticeably (R_{wp} decreased by $\sim 1\%$) if the out-of-plane (AFM) $m\Gamma_{1+}$ mode is also included, allowing the moments to cant out of the ab plane. The combination of in-plane AFM $m\Gamma_{3+}$ modes (Fig. S15a, ESI†) and an out-of-plane AFM $m\Gamma_{1+}$ mode (Fig. S15b, ESI†) give the resulting AFM structure (Fig. 9a).

The components of the moments along the $P\bar{1}$ magnetic unit cell are $a = \pm 1.256(5) \mu_{\text{B}}$, $b = \pm 1.256(5) \mu_{\text{B}}$, $c = \pm 1.59(1) \mu_{\text{B}}$. This is equivalent to components along Cartesian axes of $\mu_x = \pm 2.618(5) \mu_{\text{B}}$, $\mu_y = \pm 1.512(3) \mu_{\text{B}}$, $\mu_z = \pm 1.340(8) \mu_{\text{B}}$, giving overall

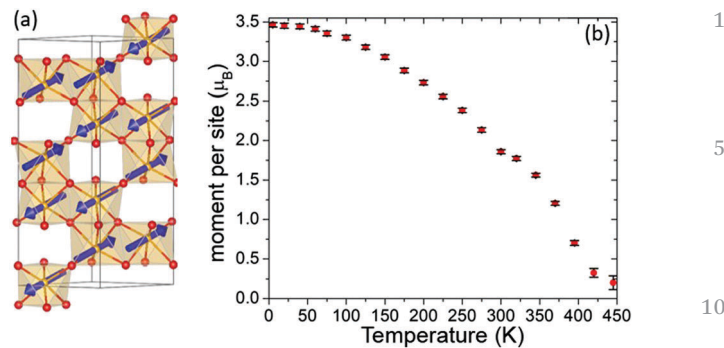


Fig. 9 (a) Magnetic structure of $\text{MnFe}_{0.5}\text{Ru}_{0.5}\text{O}_3$ at 5 K (color code: Mn/Fe/Ru = orange, O = red, magnetic moment = blue arrow). (b) Refined magnetic moment per site as a function of temperature.

an in-plane moment $\mu_{xy} = 3.023(6) \mu_{\text{B}}$ and an overall moment of $3.307(7) \mu_{\text{B}}$ per site at 5 K. The resulting ordered moment ($3.3 \mu_{\text{B}}$ at 5 K) in $\text{MnFe}_{0.5}\text{Ru}_{0.5}\text{O}_3$ is very close to that expected for a mixed $\text{Mn}^{2+}/\text{Mn}^{3+}/\text{Fe}^{3+}/\text{Ru}^{4+}$ site ($3.28 \mu_{\text{B}}$). We note that this combination of the two AFM irreducible representations (irreps) Γ_{3+} and Γ_{1+} also allows the Γ_{2+} irrep, which describes a FM component along $[001]$. Although analysis of our diffraction data does not indicate the presence of this out-of-plane FM component, we cannot exclude its presence as a secondary order parameter. However, we note that the hysteresis loop measured for $\text{MnFe}_{0.5}\text{Ru}_{0.5}\text{O}_3$ (Fig. 7b) suggests that any such component must be very small. Details from the multibank refinement at 5 K are given in Tables S4, S5 and refinement profiles are shown in Fig. 8 and Fig. S16 (ESI†).

The collinear AFM magnetic structure described here for $\text{MnFe}_{0.5}\text{Ru}_{0.5}\text{O}_3$ (Fig. 9) is similar to the collinear FiM structure reported for $\text{Mn}_2\text{FeSbO}_6$ (IL-type, $R\bar{3}$) at 150 K, in which Mn and Fe sublattices are coupled AFM in the ab plane.⁵⁷ The absence of FiM in corundum $\text{MnFe}_{0.5}\text{Ru}_{0.5}\text{O}_3$ is due to cation disorder and the absence of two AF-coupled sublattices. AFM interactions also exist in related NTO-type ($R\bar{3}$) materials such as Ni_3TeO_6 , Mn_2FeWO_6 , $\text{Mn}_2\text{FeMoO}_6$ and Mn_2MnWO_6 , which show more complicated magnetic structures as a result of three ordered metal sites leading to competition between the different magnetic sublattices.^{29,58–60} Ni_3TeO_6 exhibits a collinear AFM structure with all Ni moments along the c axis with FM honeycomb planes.^{58,59} The magnetic structure of Mn_2FeWO_6 is a collinear spin arrangement with Mn2 spins antiparallel to both Mn1 and Fe spins. In $\text{Mn}_2\text{FeMoO}_6$, a more complicated FiM is revealed with all spins parallel to the c axis but antiparallel between sub-lattices Fe, Mn1, and Mo, Mn2.²⁹ Mn_2MnWO_6 , however, adopts a non-collinear AFM magnetic structure due to frustration.⁶⁰ The canting of spins arrangement in $\text{MnFe}_{0.5}\text{Ru}_{0.5}\text{O}_3$ is also observed in the double perovskite $\text{Mn}_2\text{FeReO}_6$, where an AFM Mn lattice and a FiM Fe and Re lattice are canted away from the c axis.³⁰

The magnetic ordering temperature of $\text{MnFe}_{0.5}\text{Ru}_{0.5}\text{O}_3$ is tracked by the intensity of the magnetic-only reflections 021, 101 and 003, which smoothly decreases (Fig. S12, ESI†) as the temperature is warmed up from 5 to 445 K. Magnetic Bragg

1 reflections are clearly observed in data collected at 395 K, but
are absent at 420 K, which indicates that the transition tem-
perature of the sample is around 400 K. Sequential refinements
were then carried out with the 122° bank data which show that
5 the moment per cation site decreases smoothly from 3.46(2) μ_B
per site at 5 K to 0.70(3) μ_B per site at 395 K (Fig. 9b). The
refined magnetic moments are close to zero at 425 and 445 K, at
which no magnetic Bragg reflections are observed (Fig. S12a,
ESI†). The slight change of slope in parameters derived from
10 sequential Rietveld refinements (magnetic moment as a func-
tion of temperature, Fig. 9b; relative intensities of magnetic-
only reflections, Fig. S12, ESI†) reflects the change in heating
sequence and sample environment: NPD data were first col-
lected on heating the sample from 300 K to 450 K in vacuum
15 before the sample was cooled down to 2 K, with 150 mBar at RT
of He as exchange gas, and further data collected on heating
back up to 300 K.

Mössbauer spectroscopy

20 The experimental Mössbauer spectra of the $\text{MnFe}_{0.5}\text{Ru}_{0.5}\text{O}_3$
absorber, show that at 97 K all Fe ions are equivalent, since
all are in magnetic saturation (Fig. 10). The high field in
saturation (490 KGauss) proves that the Fe ions are all trivalent
($S = 5/2$), which is in agreement with XANES results. The low
25 temperature spectra ($T < 250$ K) were fitted with absorption
lines of Lorentzian lineshape, the absorption lines are slightly
broadened as the temperature increases.

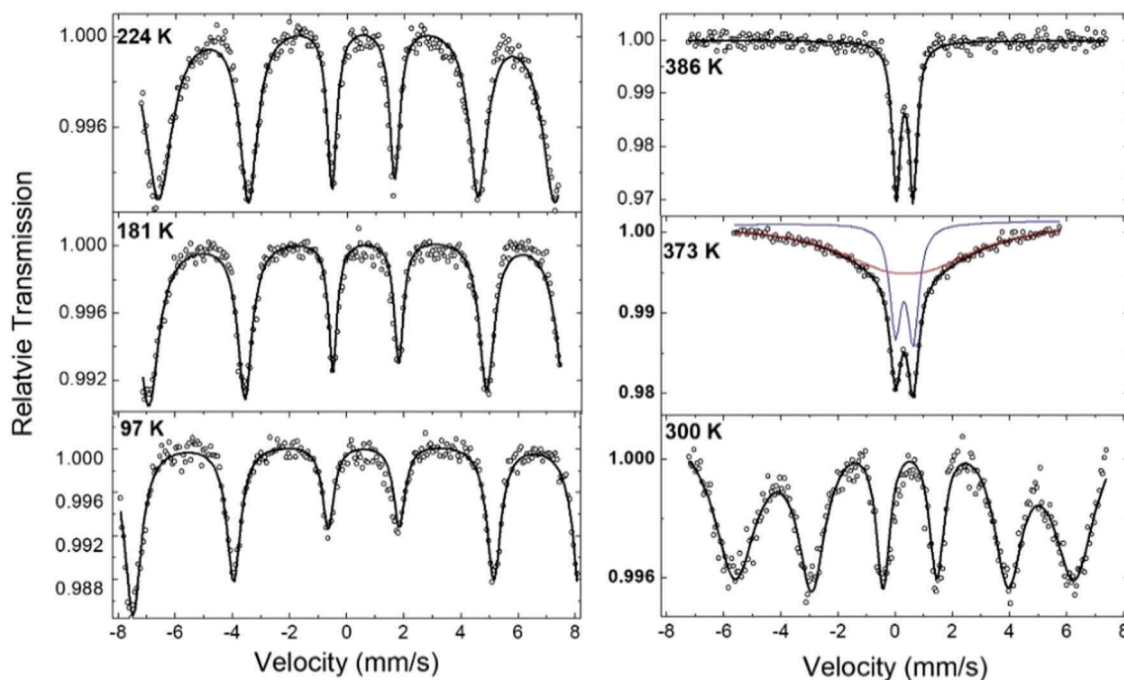
However, when the temperature is raised to above 250 K, the
absorption line widths start to broaden to a large extent, as in
30 the spectrum at 300 K (Fig. 10), and are most evident at 350 K
(Fig. S17, ESI†). The 373 K spectrum contains a mixture of a

sharp paramagnetic quadrupole doublet and a smeared mag-
netic subspectrum, which indicates that the magnetic phase
transition is not sharp (Fig. 10). At 386 K, an almost pure
quadrupole doublet with a tiny magnetic field (4 KGauss) is still
5 present. These results indicate that the Fe sublattice is already
paramagnetic above $T_C(\text{Fe}) = 390$ K, consistent with the
appearance of magnetic Bragg peaks in NPD data collected
below 395 K.

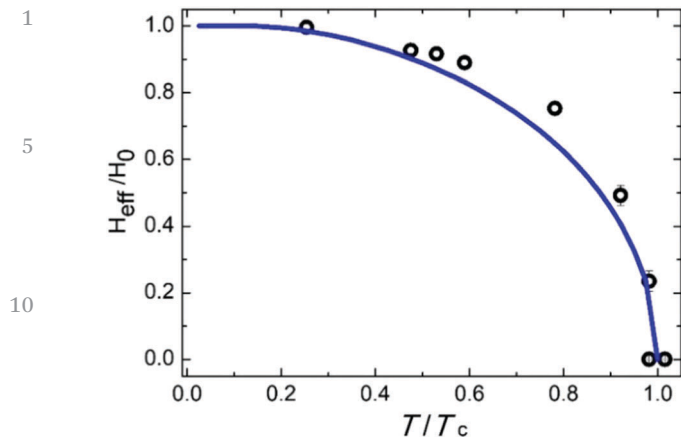
The spectra at 300 and 350 K require the presence of large
hyperfine field distribution, indicating that the Fe ions are not
all equivalent magnetically, and the spectra resemble the
features of a spin glass structure, or spin fluctuation rates in
the magnetic hyperfine splitting window. The temperature
dependence of the average hyperfine field (HF) is displayed in
Fig. 11, in terms of $\text{HF}(T/T_C)/\text{HF}(0)$, where $T_C = 390$ K and
15 $\text{HF}(0) = 490$ KGauss. The fact that the temperature dependence
of the experimental magnetic hyperfine field is quite different
from a pure magnetic Fe^{3+} sublattice, indicates that Fe ions
interact also with the Mn sublattice and possibly also with the
magnetic Ru, present also in the Fe sublattice. The broadening
20 phenomena in the Mössbauer spectra strongly support the
disordered model of Fe/Mn/Ru in corundum $\text{MnFe}_{0.5}\text{Ru}_{0.5}\text{O}_3$.

Electrical conductivity

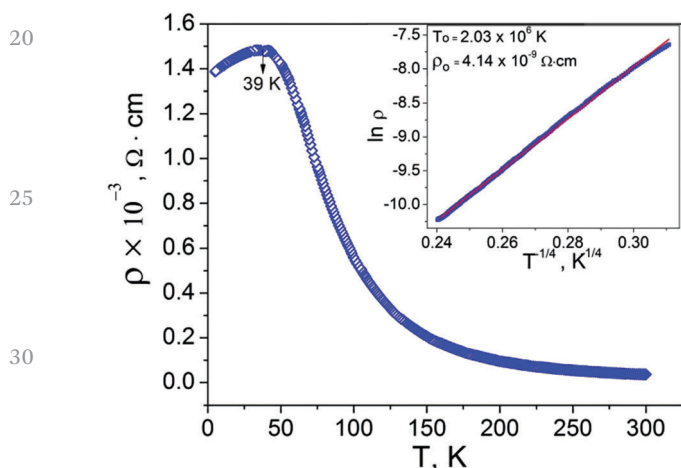
The resistivity was measured on a pellet as a function of
25 temperature between 5–300 K without applying a magnetic
field (Fig. 12). Above 40 K, the resistivity decreases as the
temperature increases, indicating semiconducting behavior.
The high temperature data between 300 and 107 K can be
linearly fitted with $\ln \rho$ versus $1/T^{1/4}$, which agrees with the
30 Mott's variable range hopping (VRH) conduction mechanism



Q4 Fig. 10 The $\text{MnFe}_{0.5}\text{Ru}_{0.5}\text{O}_3$ Mössbauer spectra at various temperatures.



15 Fig. 11 The temperature dependence ($T_C = 390$ K) of the magnetic hyperfine field in $\text{MnFe}_{0.5}\text{Ru}_{0.5}\text{O}_3$. The solid line represents a Brillouin function of $S = 5/2$.



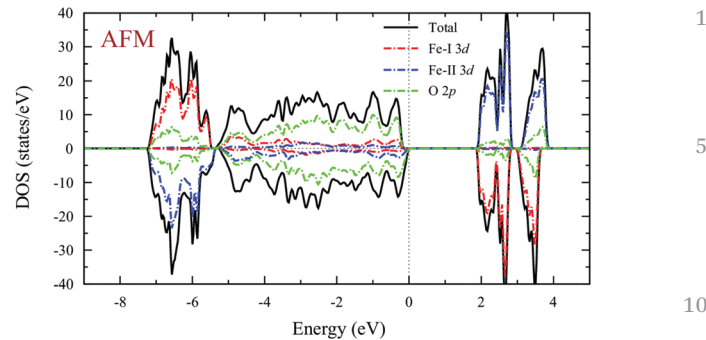
20 Fig. 12 Resistivity (ρ) as a function of temperature (T). The inset is the linear fit to the plot of $\ln \rho$ versus $1/T^{1/4}$.

$$\rho = \rho_0 \exp \left[\left(\frac{T_0}{T} \right)^{\frac{1}{4}} \right].^{61}$$

25 The fitting yields the parameters ρ_0 and T_0 equal to $4.14 \times 10^{-9} \Omega \text{ cm}$ and $2.03 \times 10^6 \text{ K}$, respectively. The high temperature resistivity behavior and the fitting results are similar to those of $\text{MnFe}_{0.5}\text{Ru}_{0.5}\text{O}_3$, a FM VRH semiconductor.²⁹ The abnormal feature around 40 K may be related to the magnetic anomaly seen in Fig. 7.

DFT calculations

30 Two possible crystal structures with $\alpha\text{-Fe}_2\text{O}_3$ type, or LN-type were discussed in the diffraction analysis. To investigate which type of crystal structure is more stable energetically, DFT was utilized. The VCA method was employed to take into account the structural disorder. In the VCA calculations, Ru disorder was assumed not to be critical to determine the stable crystal structure. Hence, Ru disorder was not considered and was simply replaced by Fe and only the Mn/Fe disorder was taken into account in the calculations. As a result, the crystal structure



35 Fig. 13 Density of states (DOS) in $\alpha\text{-Fe}_2\text{O}_3$ type crystal structure with antiferromagnetism (AFM) obtained from GGA+ U ($U = 4$ eV) calculation. The magnetic structure possesses two symmetrically different Fe sites: Fe-I and Fe-II. Black line corresponds to the total DOS. Red, blue, and green lines represent Fe-I 3d, Fe-II 3d, and O 2p partial DOS, respectively. The positive and negative values in DOS correspond to spin up and down, respectively.

with $\alpha\text{-Fe}_2\text{O}_3$ -type has lower energy than that with LN-type with an energy difference of 10.58 eV per atom. Therefore, even if Ru disorder would be considered in the VCA calculations, it would be unlikely to reverse the energy order, due to the significant energy difference, in agreement with experimental results.

30 Fig. 13 shows the density of states for antiferromagnetic ordering in the $\alpha\text{-Fe}_2\text{O}_3$ type crystal structure obtained from GGA+ U calculations. The AFM order was adopted from Fig. 9. The GGA+ U calculation with AFM order clearly shows a band gap of 1.91 eV, which supports the semiconducting behavior observed in the experiments. The magnetic structure with $\alpha\text{-Fe}_2\text{O}_3$ -type possesses two symmetrically different Fe sites and the local moments of each Fe site are 4.06, $-4.07 \mu_B$ per Fe, respectively. A weak ferromagnetic component with the magnitude of $0.004 \mu_B$ per Fe is observed in the DFT calculation, which is consistent with the experiment. In Fig. 13, the red broken line corresponds to the partial DOS for Fe-I 3d orbital. The partial DOS for Fe-I spin up is completely filled, because there is no DOS for Fe-I spin up above the Fermi level. Fe-II has the opposite occupancy. Therefore, both Fe-I and Fe-II show Fe^{3+} (d^5) with high spin configuration. In comparing the total energies of AFM and FM states in the GGA+ U calculations, the AFM state has a lower energy by 0.098 eV per atom from that of the FM state.

Comparison of $\text{MnFe}_{0.5}\text{Ru}_{0.5}\text{O}_3$ and related $\text{Mn}_2\text{BB}'\text{O}_6$

35 To date, eight transition-metal-only $\text{A}_2\text{BB}'\text{O}_6$ ($A = \text{Mn}$, $B = \text{Fe}$, Mn , $B' = \text{Nb}$, Ta , W , Re) oxides have been successfully prepared under high pressure (5–8 GPa) and high temperature (1573–1875 K) (Table 3). While $\text{Mn}_2\text{MnReO}_6$ and $\text{Mn}_2\text{FeReO}_6$ form highly distorted DP (AO_8 with rock salt ordering of corner-linked BO_6 and $\text{B}'\text{O}_6$), other $\text{A}_2\text{BB}'\text{O}_6$ oxides form cation-ordered, noncentrosymmetric corundum derivatives, such as the LN and NTO phases (with face- and corner-linked six-coordinated AO_6 , BO_6 and $\text{B}'\text{O}_6$ octahedra). In $\text{Mn}_2\text{FeNbO}_6$ and $\text{Mn}_2\text{FeTaO}_6$, the B and B' sites disorder due to the small size difference between Fe^{3+} and Nb^{5+} ions (0.005 Å), but the overall structure, with ordering of large Mn^{2+} ions on the A

Table 3 Comparison of transition-metal-only $A_2BB'O_6$

| Compound | Synthesis | A, d^n , r^{62} | B, d^n , r | B', d^n , r | Structure | T_C/T_N , K |
|---|---|---|---|--|--|--------------------------------|
| Mn_2FeNbO_6 ²⁸ | MnO + Fe ₂ O ₃ + Nb ₂ O ₅ , 1573 K, 7 GPa | Mn ²⁺ , 3d ⁵ 0.83 Å | Fe ³⁺ , 3d ⁵ 0.645 Å | Nb ⁵⁺ , 4d ⁰ 0.64 Å | LN, $R3c$ | $T_N = 90$, $T_C \sim 200$ |
| Mn_2FeTaO_6 ²⁸ | MnO + Fe ₂ O ₃ + Ta ₂ O ₅ , 1573 K, 7 GPa | Mn ²⁺ , 3d ⁵ 0.83 Å | Fe ³⁺ , 3d ⁵ 0.645 Å | Ta ⁵⁺ , 5d ⁰ 0.64 Å | LN, $R3c$ | $T_N = 80$, $T_C \sim 200$ |
| Mn_2FeWO_6 ³¹ | MnO + Fe ₂ O ₃ + Fe + WO ₃ , 1673 K, 8 GPa | Mn ²⁺ , 3d ⁵ 0.83 Å | Fe ²⁺ , 3d ⁶ 0.78 Å | W ⁶⁺ , 5d ⁰ 0.60 Å | NTO, $R3$ | $T_N = 75$ |
| Mn_2FeMoO_6 ²⁹ | MnO + Fe ₂ O ₃ + Fe + MoO ₃ , 1623 K, 8 GPa | Mn ²⁺ , 3d ⁵ 0.83 Å | Fe ³⁺ , 3d ⁵ 0.645 Å | Mo ⁵⁺ , 4d ¹ 0.61 Å | NTO, $R3$ | $T_C = 337$ |
| $Mn_2(Fe_{0.8}Mo_{0.2})MoO_6$ ⁶³ | MnO + Fe ₂ O ₃ + Fe + MoO ₃ , 1623 K, 8 GPa | Mn ²⁺ , 3d ⁵ 0.83 Å | Fe ³⁺ , 3d ⁵ 0.645 Å | Mo ^{4/5+} , 4d ^{2/1} 0.65/0.61 Å | DP, $P2_1/n$ | $T_C = 194$ |
| Mn_2FeReO_6 ³⁰ | MnO + Fe ₂ O ₃ + Fe + ReO ₃ , 1873 K, 5 GPa | Mn ²⁺ , 3d ⁵ 0.83 Å | Fe ³⁺ , 3d ⁵ 0.645 Å | Re ⁵⁺ , 5d ² 0.58 Å | DP, $P2_1/n$ | $T_C = 520$ |
| $MnFe_{0.5}Ru_{0.5}O_3$ | MnO + MnO ₂ + Fe ₂ O ₃ + RuO ₂ , 1623 K, 5 GPa | Mn ^{2+/3+} , 3d ^{5/4} 0.83/0.645 Å | Fe ³⁺ , 3d ⁵ 0.645 Å | Ru ^{3/4+} , 4d ^{5/4} 0.562/0.62 Å | α -Fe ₂ O ₃ , $R\bar{3}c$ | $T_N \sim 400$ |
| Mn_2MnWO_6 ⁶⁰ | MnO + WO ₃ , 1673 K, 8 GPa | Mn ²⁺ , 3d ⁵ 0.83 Å | Mn ²⁺ , 3d ⁵ 0.83 Å | W ⁶⁺ , 5d ¹ 0.60 Å | NTO, $R3$ | $T_N = 58$ |
| Mn_2MnReO_6 ⁶⁴ | MnO + ReO ₃ , 1673 K, 5 GPa | Mn ²⁺ , 3d ⁵ 0.83 Å | Mn ^{2+/3+} , 3d ^{5/4} 0.83/0.645 Å | Re ^{5+/6+} , 5d ^{2/1} 0.58/0.55 Å | DP, $P2_1/n$ | $T_N = 110$ |

sites, is still polar LN-type which is stabilized by the second-order Jahn–Teller effect of d⁰ Nb⁵⁺/Ta⁵⁺ ions. Mn_2FeWO_6 and Mn_2MnWO_6 crystallize in the NTO-type structure with ordered B and B' sites due to the large charge difference (4) and size difference (0.23 Å) between Fe²⁺ and W⁶⁺ ions. Although the charge difference (2) and size difference (0.035 Å) between Fe³⁺ and Mo⁵⁺ are small, Mn_2FeMoO_6 surprisingly also stabilizes in the NTO-type structure, which is attributed to FiM magnetic configuration that leads to the lowest energy state.

$MnFe_{0.5}Ru_{0.5}O_3$ is the first example of transition-metal-only $A_2BB'O_6$ phase that adopts the corundum structure with totally disordered A, B, and B' sites (Table 3). This lack of cation order is thought to arise due to the small size and charge difference between Mn^{2+/3+}, Fe³⁺ and Ru^{3+/4+}. The mixed-valence of Mn^{2+/3+} and disorder in $MnFe_{0.5}Ru_{0.5}O_3$ is also likely related to the strong Jahn–Teller effect of Mn³⁺ (3d⁴), which is not favorable for face, or edge-sharing octahedra in corundum-related structures. The failure to oxidize Ru⁴⁺ to Ru⁵⁺ with MnO₂ during the synthesis causes $MnFe_{0.5}Ru_{0.5}O_3$ to stabilize in the non-polar corundum phase instead of DP, polar LN, or NTO phases. Ru⁵⁺ in this phase may be achieved by optimizing synthetic conditions *e.g.*, with use of an oxidizing agent as KClO₃ or KClO₄, which converts to a KCl byproduct that can be easily washed away by water after the reaction.

The magnetic properties of $MnFe_{0.5}Ru_{0.5}O_3$ are different from those reported for $Mn_2FeB'O_6$. $Mn_2FeB'O_6$ (B' = Nb⁵⁺, Ta⁵⁺, W⁵⁺) shows clear AFM ordering between 75–90 K, with weak FM ~ 210 K for B' = Nb⁵⁺, Ta⁵⁺ (Table 3) while Mn_2FeMoO_6 and Mn_2FeReO_6 exhibit FiM ordering above RT. The introduction of more dⁿ ($n > 0$) electrons at the B'-sites of $Mn_2FeB'O_6$ (B' = Mo⁵⁺, Re⁵⁺) changes the AFM to FiM ordering and also increases the ordering temperature dramatically. The ideal $Mn_2^{2+}Fe^{3+}Ru^{5+}O_6$ with an ordered polar structure is expected to show FM.

Conclusions

$MnFe_{0.5}Ru_{0.5}O_3$ is the first example of a cation-disordered corundum-derived oxide in the transition-metal-only $A_2BB'O_6$

series, which is synthesized by high pressure and high temperature. X-ray absorption K- and L-near edge spectroscopies establish mixed-valent Mn^{2+/3+}, Fe³⁺ and Ru^{~4+} formal oxidation states. The similar cation sizes and charges of metal ions provide a smaller driving force for ordering than in related systems containing small and highly charged B/B' ions along with a high content of the large A-site Mn²⁺ ion. This is reflected in the unit cell parameters and bond lengths, with a much smaller in-plane parameter (and unit cell volume) and shorter M–O bond lengths for $MnFe_{0.5}Ru_{0.5}O_3$ compared with ordered analogues such as $Mn_2FeB'O_6$ (B' = Nb⁵⁺, Ta⁵⁺, W⁶⁺) and $Mn_2Mn^{2+}W^{6+}O_6$, which all possess a much higher content of the large Mn²⁺ ion. This suggests that to design new cation-ordered corundum-derived materials, care must be taken to ensure the redox chemistry of the system to allow for a large A cation (such as Mn²⁺, Zn²⁺) with much smaller and more highly charged B/B' cations.

Analysis of the cation distribution in $MnFe_{0.5}Ru_{0.5}O_3$ highlights the importance of using several complementary structural characterization methods to confirm the symmetry and structure; neither XRPD nor NPD alone allowed the unambiguous determination of the disordered distribution of Mn, Fe and Ru ions. However, the similar X-ray scattering lengths of Mn and Fe, in contrast to the much heavier Ru combined with the very different neutron scattering lengths of Mn and Fe lead to the establishment of the cation-disordered $R\bar{3}c$ nuclear structure. This disordered model is consistent with transmission electron microscopy, XANES, and Mössbauer spectra results. The centrosymmetric nature is also confirmed by the absence of SHG signal.

NPD analysis confirms a collinear AFM magnetic structure (with moments in general direction) with $T_N \sim 400$ K, which is in agreement with temperature-dependent magnetic and Mössbauer spectra results. The corundum structure and AFM ground state are supported by theoretical calculations. As a semiconductor with an ordering temperature above RT, $MnFe_{0.5}Ru_{0.5}O_3$ may be a potential candidate for spintronic applications.

Conflicts of interest

Q5

Acknowledgements

M. G. thanks the NSF-DMR-1507252 grant of the United States. X. T., G. K. and C. J. K. were supported by the “Center for Computational Design of Functional Strongly Correlated Materials and Theoretical Spectroscopy” under DOE Grant No. DE-FOA-0001276. MRCAT operations are supported by the Department of Energy and the MRCAT member institutions. EEM is grateful to the Leverhulme Trust (RPG-2017-362). M. R. Li and M. X. Wu are supported by the “One Thousand Youth Talents” Program of China. Use of the Advanced Photon Source at Argonne National Laboratory was supported by the U. S. Department of Energy, Office of Science, Office of Basic Energy Sciences, under Contract No. DE-AC02-06CH11357. Part of this research used the ISS, 8-ID and TES, 8-BM beamlines at the National Synchrotron Light Source II (NSLS-II), a U.S. Department of Energy (DOE) Office of Science User Facility operated for the DOE Office of Science by Brookhaven National Laboratory under Contract No. DE-SC0012704. Without the valuable aid/support of the NSLS-II staff scientists Eli Stavitski, Klaus Attenkofer, and Paul Northrup this phase of the work could not have been performed. The work at IOPCAS was supported by NSF & MOST of China through research projects. H. R. and V. G. acknowledge NSF-MRSEC Center for Nanoscale Science at Penn State through the grant number DMR-1820620. The authors would like to thank Ms Jean Hanley at Lamont-Doherty Earth Observatory in Columbia University for making the high-pressure assemblies. The authors acknowledge the science and technology facility council (STFC) UK for the provision of neutron beam time. The authors would like to thank Daniel Nye for help on the Rigaku SmartLab X-ray diffractometer instrument in the Materials Characterization Laboratory at the ISIS Neutron and Muon Source.

References

- S. A. Wolf, D. D. Awschalom, R. A. Buhrman, J. M. Daughton, S. von Molnar, M. L. Roukes, A. Y. Chtchelkanova and D. M. Treger, *Science*, 2001, **294**, 1488–1495.
- C. Chappert, A. Fert and F. N. Van Dau, *Nat. Mater.*, 2007, **6**, 813–823.
- C. Felser, G. H. Fecher and B. Balke, *Angew. Chem., Int. Ed. Engl.*, 2007, **46**, 668–699.
- A. P. Ramirez, R. J. Cava and J. Krajewski, *Nature*, 1997, **386**, 156–159.
- W. Kobayashi, S. Ishiwata, I. Terasaki, M. Takano, I. Grigorovičute, H. Yamauchi and M. Karppinen, *Phys. Rev. B: Condens. Matter Mater. Phys.*, 2005, **72**, 104408.
- T. Katase, H. Takahashi, T. Tohei, Y. Suzuki, M. Yamanouchi, Y. Ikuhara, I. Terasaki and H. Ohta, *Adv. Electron. Mater.*, 2015, **1**, 1500199.
- N. S. Rogado, J. Li, A. W. Sleight and M. A. Subramanian, *Adv. Mater.*, 2005, **17**, 2225–2227.
- R. I. Dass, J. Q. Yan and J. B. Goodenough, *Phys. Rev. B: Condens. Matter Mater. Phys.*, 2003, **68**, 064415.
- Y. Krockenberger, K. Mogare, M. Reehuis, M. Tovar, M. Jansen, G. Vaitheeswaran, V. Kanchana, F. Bultmark, A. Delin, F. Wilhelm, A. Rogalev, A. Winkler and L. Alff, *Phys. Rev. B: Condens. Matter Mater. Phys.*, 2007, **75**, 020404.
- B. G. Park, J. Wunderlich, X. Marti, V. Holy, Y. Kurosaki, M. Yamada, H. Yamamoto, A. Nishide, J. Hayakawa, H. Takahashi, A. B. Shick and T. Jungwirth, *Nat. Mater.*, 2011, **10**, 347–351.
- A. B. Shick, S. Khmelevskiy, O. N. Mryasov, J. Wunderlich and T. Jungwirth, *Phys. Rev. B: Condens. Matter Mater. Phys.*, 2010, **81**, 212409.
- R. Duine, *Nat. Mater.*, 2011, **10**, 344–345.
- T. Jungwirth, X. Marti, P. Wadley and J. Wunderlich, *Nat. Nanotechnol.*, 2016, **11**, 231–241.
- C. Marrows, *Science*, 2016, **351**, 558–559.
- P. Wadley, B. Howells, J. Zelezny, C. Andrews, V. Hills, R. P. Campion, V. Novak, K. Olejnik, F. Maccherozzi, S. S. Dhesi, S. Y. Martin, T. Wagner, J. Wunderlich, F. Freimuth, Y. Mokrousov, J. Kunes, J. S. Chauhan, M. J. Grzybowski, A. W. Rushforth, K. W. Edmonds, B. L. Gallagher and T. Jungwirth, *Science*, 2016, **351**, 587–590.
- O. Gomonay, T. Jungwirth and J. Sinova, *Phys. Status Solidi RRL*, 2017, **11**, 1700022.
- V. Baltz, A. Manchon, M. Tsoi, T. Moriyama, T. Ono and Y. Tserkovnyak, *Rev. Mod. Phys.*, 2018, **90**, 015005.
- T. Jungwirth, J. Sinova, A. Manchon, X. Marti, J. Wunderlich and C. Felser, *Nat. Phys.*, 2018, **14**, 200–203.
- P. Němec, M. Fiebig, T. Kampfrath and A. V. Kimel, *Nat. Phys.*, 2018, **14**, 229–241.
- R. A. Duine, K.-J. Lee, S. S. P. Parkin and M. D. Stiles, *Nat. Phys.*, 2018, **14**, 217–219.
- A. Beleanu, J. Kiss, G. Kreiner, C. Köhler, L. MÜchler, W. Schnelle, U. Burkhardt, S. Chadov, S. Medvediev, D. Ebke, C. Felser, G. Cordier, B. Albert, A. Hoser, F. Bernardi, T. I. Larkin, D. Pröpper, A. V. Boris and B. Keimer, *Phys. Rev. B: Condens. Matter Mater. Phys.*, 2013, **88**, 184429.
- P. Wadley, V. Novak, R. P. Campion, C. Rinaldi, X. Marti, H. Reichlova, J. Zelezny, J. Gazquez, M. A. Roldan, M. Varela, D. Khalyavin, S. Langridge, D. Kriegner, F. Maca, J. Masek, R. Bertacco, V. Holy, A. W. Rushforth, K. W. Edmonds, B. L. Gallagher, C. T. Foxon, J. Wunderlich and T. Jungwirth, *Nat. Commun.*, 2013, **4**, 2322.
- J. Mundelein and H. U. Schuster, *Z. Naturforsch. B*, 1992, **47**, 925–928.
- X. Marti, I. Fina, C. Frontera, J. Liu, P. Wadley, Q. He, R. J. Paull, J. D. Clarkson, J. Kudrnovsky, I. Turek, J. Kunes, D. Yi, J. H. Chu, C. T. Nelson, L. You, E. Arenholz, S. Salahuddin, J. Fontcuberta, T. Jungwirth and R. Ramesh, *Nat. Mater.*, 2014, **13**, 367–374.
- D. Kriegner, K. Vyborny, K. Olejnik, H. Reichlova, V. Novak, X. Marti, J. Gazquez, V. Saidl, P. Nemeč, V. V. Volobuev, G. Springholz, V. Holy and T. Jungwirth, *Nat. Commun.*, 2016, **7**, 11623.

- 1 26 I. Fina, X. Marti, D. Yi, J. Liu, J. H. Chu, C. Rayan-Serrao, S. Suresha, A. B. Shick, J. Zelezny, T. Jungwirth, J. Fontcuberta and R. Ramesh, *Nat. Commun.*, 2014, **5**, 4671.
- 27 B. J. Kim, H. Ohsumi, T. Komesu, S. Sakai, T. Morita, H. Takagi and T. Arima, *Science*, 2009, **323**, 1329–1332.
- 5 28 M.-R. Li, D. Walker, M. Retuerto, T. Sarkar, J. Hadermann, P. W. Stephens, M. Croft, A. Ignatov, C. P. Grams, J. Hemberger, I. Nowik, P. S. Halasyamani, T. T. Tran, S. Mukherjee, T. S. Dasgupta and M. Greenblatt, *Angew. Chem., Int. Ed. Engl.*, 2013, **52**, 8406–8410.
- 10 29 M.-R. Li, M. Retuerto, D. Walker, T. Sarkar, P. W. Stephens, S. Mukherjee, T. S. Dasgupta, J. P. Hodges, M. Croft, C. P. Grams, J. Hemberger, J. Sanchez-Benitez, A. Huq, F. O. Saouma, J. I. Jang and M. Greenblatt, *Angew. Chem., Int. Ed. Engl.*, 2014, **53**, 10774–10778.
- 15 30 M.-R. Li, M. Retuerto, Z. Deng, P. W. Stephens, M. Croft, Q. Huang, H. Wu, X. Deng, G. Kotliar, J. Sanchez-Benitez, J. Hadermann, D. Walker and M. Greenblatt, *Angew. Chem., Int. Ed. Engl.*, 2015, **54**, 12069–12073.
- 20 31 M.-R. Li, M. Croft, P. W. Stephens, M. Ye, D. Vanderbilt, M. Retuerto, Z. Deng, C. P. Grams, J. Hemberger, J. Hadermann, W. M. Li, C. Q. Jin, F. O. Saouma, J. I. Jang, H. Akamatsu, V. Gopalan, D. Walker and M. Greenblatt, *Adv. Mater.*, 2015, **27**, 2177–2181.
- 25 32 L. C. Chapon, P. Manuel, P. G. Radaelli, C. Benson, L. Perrott, S. Ansell, N. J. Rhodes, D. Raspino, D. Duxbury, E. Spill and J. Norris, *J. Neutron News*, 2011, **22**, 22.
- 33 A. A. Coelho, *J. Appl. Crystallogr.*, 2003, **36**, 86.
- 34 A. A. Coelho, *Topas Academic*, Bruker AXS, Karlsruhe, Germany, 5th edn, 2012.
- 30 35 B. J. Campbell, H. T. Stokes, D. E. Tanner and D. M. Hatch, *J. Appl. Crystallogr.*, 2006, **39**, 607–614.
- 36 C. Koch, PhD thesis, Arizona State University, 2002.
- 37 L. Bellaiche and D. Vanderbilt, *Phys. Rev. B: Condens. Matter Mater. Phys.*, 2000, **61**, 7877–7882.
- 35 38 P. Giannozzi, S. Baroni, N. Bonini, M. Calandra, R. Car, C. Cavazzoni, D. Ceresoli, G. L. Chiarotti, M. Cococcioni, I. Dabo, A. Dal Corso, S. de Gironcoli, S. Fabris, G. Fratesi, R. Gebauer, U. Gerstmann, C. Gougoussis, A. Kokalj, M. Lazzeri, L. Martin-Samos, N. Marzari, F. Mauri, R. Mazzarello, S. Paolini, A. Pasquarello, L. Paulatto, C. Sbraccia, S. Scandolo, G. Sclauzero, A. P. Seitsonen, A. Smogunov, P. Umari and R. M. Wentzcovitch, *J. Phys.: Condens. Matter*, 2009, **21**, 395502.
- 45 39 P. Giannozzi, O. Andreussi, T. Brumme, O. Bunau, M. B. Nardelli, M. Calandra, R. Car, C. Cavazzoni, D. Ceresoli, M. Cococcioni, N. Colonna, I. Carnimeo, A. Dal Corso, S. de Gironcoli, P. Delugas, R. A. DiStasio, A. Ferretti, A. Floris, G. Fratesi, G. Fugallo, R. Gebauer, U. Gerstmann, F. Giustino, T. Gorni, J. Jia, M. Kawamura, H. Y. Ko, A. Kokalj, E. Kucukbenli, M. Lazzeri, M. Marsili, N. Marzari, F. Mauri, N. L. Nguyen, H. V. Nguyen, A. Otero-de-la-Roza, L. Paulatto, S. Ponce, D. Rocca, R. Sabatini, B. Santra, M. Schlipf, A. P. Seitsonen, A. Smogunov, I. Timrov, T. Thonhauser, P. Umari, N. Vast, X. Wu and S. Baroni, *J. Phys.: Condens. Matter*, 2017, **29**, 465901.
- 40 D. Vanderbilt, *Phys. Rev. B: Condens. Matter Mater. Phys.*, 1990, **41**, 7892–7895.
- 41 P. Blaha, K. Schwarz, G. K. H. Madsen, D. Kvasnicka and J. Luitz, *WIEN2k*, Technische Universität Wien, Wien, Austria, 2001.
- 5 42 J. P. Perdew, K. Burke and M. Ernzerhof, *Phys. Rev. Lett.*, 1996, **77**, 3865–3868.
- 43 V. I. Anisimov, I. V. Solovyev, M. A. Korotin, M. T. Czyzyk and G. A. Sawatzky, *Phys. Rev. B: Condens. Matter Mater. Phys.*, 1993, **48**, 16929–16934.
- 10 44 V. I. Anisimov, F. Aryasetiawan and A. I. Lichtenstein, *J. Phys.: Condens. Matter*, 1997, **9**, 767–808.
- 45 G.-H. Cai, M. Greenblatt and M.-R. Li, *Chem. Mater.*, 2017, **29**, 5447–5457.
- 46 V. F. Sears, *Neutron News*, 1990, **3**, 29–37.
- 15 47 S. A. Denev, T. T. A. Lummen, E. Barnes, A. Kumar and V. Gopalan, *J. Am. Ceram. Soc.*, 2011, **94**, 2699–2727.
- 48 F. M. F. de Groot, Z. W. Hu, M. F. Lopez, G. Kaindl, F. Guillot and M. Tronc, *J. Chem. Phys.*, 1994, **101**, 6570–6576.
- 20 49 K. V. Ramanujachary, S. E. Lofland, W. H. McCarroll, T. J. Emge, M. Greenblatt and M. Croft, *J. Solid State Chem.*, 2002, **164**, 60–70.
- 50 F. D. Groot, *Coord. Chem. Rev.*, 2005, **249**, 31–63.
- 25 51 G. M. Veith, M. Greenblatt, M. Croft, K. V. Ramanujachary, J. Hattrick-Simpers, S. E. Lofland and I. Nowik, *Chem. Mater.*, 2005, **17**, 2562–2567.
- 52 R. O. Bune, M. V. Lobanov, G. Popov, M. Greenblatt, C. E. Botez, P. W. Stephens, M. Croft, J. Hadermann and G. Van Tendeloo, *Chem. Mater.*, 2006, **18**, 2611–2617.
- 30 53 M. Retuerto, M.-R. Li, Y. B. Go, A. Ignatov, M. Croft, K. V. Ramanujachary, J. Hadermann, J. P. Hodges, R. H. Herber, I. Nowik and M. Greenblatt, *Inorg. Chem.*, 2012, **51**, 12273–12280.
- 54 Z. Hu, H. von Lips, M. S. Golden, J. Fink, G. Kaindl, F. M. F. de Groot, S. Ebbinghaus and A. Reller, *Phys. Rev. B: Condens. Matter Mater. Phys.*, 2000, **61**, 5262–5266.
- 55 R. Nepal, Q. Zhang, S. Dai, W. Tian, S. E. Nagler and R. Jin, *Phys. Rev. B: Condens. Matter Mater. Phys.*, 2018, **97**, 024410.
- 40 56 M. C. Kemei, J. K. Harada, R. Seshadri and M. R. Suchumel, *Phys. Rev. B: Condens. Matter Mater. Phys.*, 2014, **90**, 064418.
- 57 A. J. Dos santos-García, E. Solana-Madruga, C. Ritter, A. Andrada-Chacón, J. Sánchez-Benítez, F. J. Mompean, M. Garcia-Hernandez, R. Sáez-Puche and R. Schmidt, *Angew. Chem., Int. Ed.*, 2017, **56**, 4438–4442.
- 45 58 I. Zivkovic, K. Prsa, O. Zaharko and H. Berger, *J. Phys.: Condens. Matter*, 2010, **22**, 056002.
- 59 Y. S. Oh, S. Artyukhin, J. J. Yang, V. Zapf, J. W. Kim, D. Vanderbilt and S. W. Cheong, *Nat. Commun.*, 2014, **5**, 3201.
- 50 60 M.-R. Li, E. E. McCabe, P. W. Stephens, M. Croft, L. Collins, S. V. Kalinin, Z. Deng, M. Retuerto, A. Sen Gupta, H. Padmanabhan, V. Gopalan, C. P. Grams, J. Hemberger, F. Orlandi, P. Manuel, W. M. Li, C. Q. Jin, D. Walker and M. Greenblatt, *Nat. Commun.*, 2017, **8**, 2037.
- 55

- 1 61 N. F. Mott, *Conduction in Non-Crystalline Materials*, Clarendon Press, Oxford, 2nd edn, 1993.
- 62 R. D. Shannon, *Acta Crystallogr., Sect. A: Cryst. Phys., Diffr., Theor. Gen. Crystallogr.*, 1976, **32**, 751.
- 5 63 M.-R. Li, P. W. Stephens, M. Croft, Z. Deng, W. Li, C. Jin, M. Retuerto, J. P. Hodges, C. E. Frank, M. Wu, D. Walker and M. Greenblatt, *Chem. Mater.*, 2018, **30**, 4508–4514.
- 64 M.-R. Li, J. P. Hodges, M. Retuerto, Z. Deng, P. W. Stephens, M. C. Croft, X. Deng, G. Kotliar, J. Sánchez-Benítez, D. Walker and M. Greenblatt, *Chem. Mater.*, 2016, **28**, 3148–3158.
- 10
- 15
- 20
- 25
- 30
- 35
- 40
- 45
- 50
- 55